Article

Cell

Cryo-EM Structure of the Human Cannabinoid Receptor CB2-G_i Signaling Complex

Graphical Abstract

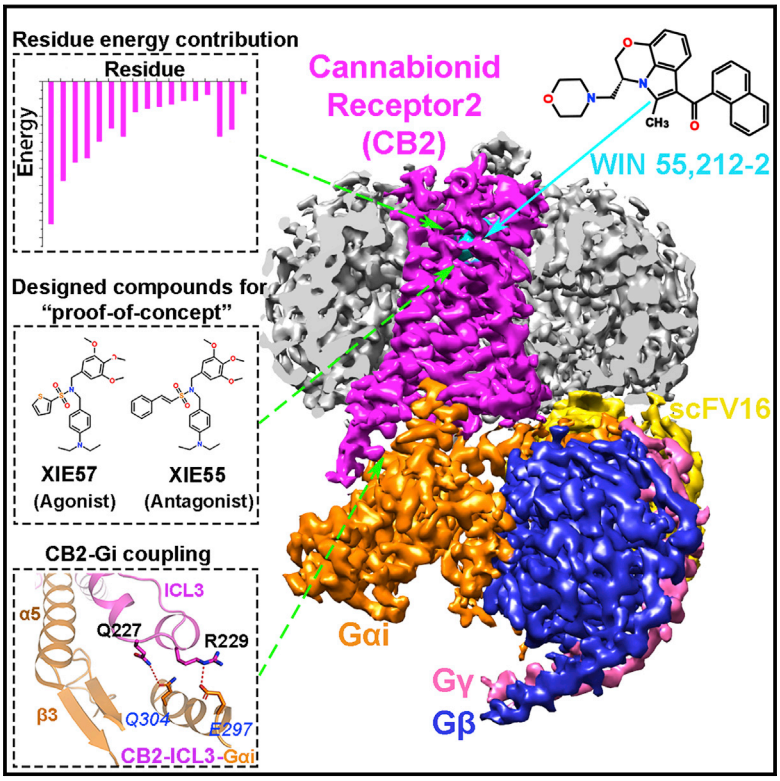

Highlights

- 3.2-Å cryo-EM structure of the CB2-G_i complex bound to potent agonist WIN 55,212-2
- Algorithm developed for quantitative characterization of binding residues
- Structural determinants for distinguishing CB2 agonists from antagonists
- CB2-Gi binding features and different activation mechanisms of CB2 and CB1

Authors

Changrui Xing, Youwen Zhuang, Ting-Hai Xu, ..., Cheng Zhang, H. Eric Xu, Xiang-Qun Xie

Correspondence

chengzh@pitt.edu (C.Z.), eric.xu@simm.ac.cn (H.E.X.), xix15@pitt.edu (X.-Q.X.)

In Brief

The 3D structure of the agonist-bound CB2-G_i signaling complex provides insight into the key residues involved in ligand recognition and the distinction of agonists and antagonists critical for facilitating rational design of drugs targeting the cannabinoid system.

Xing et al., 2020, Cell *180*, 645–654
February 20, 2020
https://doi.org/10.1016/j.cell.2020.01.007

CellPress

Cell

Cryo-EM Structure of the Human Cannabinoid Receptor CB2-G_i Signaling Complex

Changrui Xing,[1,2,9] Youwen Zhuang,[3,4,5,9] Ting-Hai Xu,[5,9] Zhiwei Feng,[1,2,9] X. Edward Zhou,[5] Maozi Chen,[1] Lei Wang,[6] Xing Meng,[7] Ying Xue,[1,8] Junmei Wang,[1] Heng Liu,[6] Terence Francis McGuire,[1] Gongpu Zhao,[7] Karsten Melcher,[5] Cheng Zhang,[6,*] H. Eric Xu,[3,*] and Xiang-Qun Xie[1,2,10,*]

[1]Department of Pharmaceutical Sciences, Computational Chemical Genomics Screen Center, School of Pharmacy, and NIDA National Center of Excellence for Computational Drug Abuse Research, University of Pittsburgh, Pittsburgh, PA 15261, USA

[2]Drug Discovery Institute and Departments of Computational Biology and of Structural Biology, University of Pittsburgh, Pittsburgh, PA 15261, USA

[3]CAS Key Laboratory of Receptor Research, Shanghai Institute of Materia Medica, Chinese Academy of Sciences, Shanghai 201203, China

[4]University of the Chinese Academy of Sciences, Beijing 100049, China

[5]Center for Cancer and Cell Biology, Program for Structural Biology, Van Andel Institute, Grand Rapids, MI 49503, USA

[6]Laboratory for GPCR Biology, Department of Pharmacology and Chemical Biology, School of Medicine, University of Pittsburgh, Pittsburgh, PA 15261, USA

[7]David Van Andel Advanced Cryo-Electron Microscopy Suite, Van Andel Research Institute, Grand Rapids, MI 49503, USA

[8]Department of Pharmacy and Therapeutics, School of Pharmacy, University of Pittsburgh, Pittsburgh, PA 15261, USA

[9]These authors contributed equally

[10]Lead Contact

*Correspondence: chengzh@pitt.edu (C.Z.), eric.xu@simm.ac.cn (H.E.X.), xix15@pitt.edu (X.-Q.X.)

https://doi.org/10.1016/j.cell.2020.01.007

SUMMARY

Drugs selectively targeting CB2 hold promise for treating neurodegenerative disorders, inflammation, and pain while avoiding psychotropic side effects mediated by CB1. The mechanisms underlying CB2 activation and signaling are poorly understood but critical for drug design. Here we report the cryo-EM structure of the human CB2-G_i signaling complex bound to the agonist WIN 55,212-2. The 3D structure reveals the binding mode of WIN 55,212-2 and structural determinants for distinguishing CB2 agonists from antagonists, which are supported by a pair of rationally designed agonist and antagonist. Further structural analyses with computational docking results uncover the differences between CB2 and CB1 in receptor activation, ligand recognition, and G_i coupling. These findings are expected to facilitate rational structure-based discovery of drugs targeting the cannabinoid system.

INTRODUCTION

The endocannabinoid system (ECS) includes two major G protein-coupled receptors (GPCRs), cannabinoid receptor subtypes 1 and 2 (CB1 and CB2), which mediate the biophysiological activities of the phytocannabinoid Δ9-tetrahydrocannabinol (THC) and several endogenous cannabinoids. ECS is a complex and homeostatic system that is involved in a broad spectrum of physiological and pathological processes such as appetite regulation (Kirkham, 2005), peripheral energy metabolism (Seeley and Woods, 2003), pain and inflammation (Calignano et al., 1998; Walter and Stella, 2004), cardiovascular regulation (Fulmer and Thewke, 2018), musculoskeletal disorders (Idris and Ralston, 2012), and cancer (Śledziński et al., 2018). Efforts have been made to develop selective CB1 and CB2 ligands that can modulate these biological functions and treat associated diseases. Although some CB2-selective agonists have been developed, showing certain efficacy in animal models or *in vitro* assays (Leleu-Chavain et al., 2019; Nettekoven et al., 2016; Scott et al., 2019; Mukhopadhyay et al., 2016; Mugnaini et al., 2019), there are no such drugs on the market for clinical use besides the phytocannabinoids and their analogs (Maroon and Bost, 2018; Yang et al., 2012b).

As a therapeutic target, CB2 has a notable advantage over CB1 in its pattern of expression. CB1 is primarily expressed in the central nervous system (CNS) and is the primary receptor responsible for the psychotropic effects of THC and the deleterious psychiatric side effects of CB1-targeting drugs. The CB1 inverse agonists rimonabant and taranabant (MK-0364) were developed as anti-obesity drugs, but both produce crippling CNS side effects of anxiety, depression, and suicidal ideation (Aronne et al., 2010; Proietto et al., 2010; Moreira and Crippa, 2009), and were consequently either withdrawn from the market or dropped in clinical trials. In contrast, CB2 is predominantly expressed in peripheral tissues of the immune system, such as the spleen and thymus, where it modulates immune suppression, apoptosis, and cell migration (Yang et al., 2012a; Galiègue et al., 1995). Modest levels of CB2 expression have also been observed in several areas of the brain, such as ventral tegmental area dopamine neurons and hippocampal CA3 neurons (Onaivi et al., 2006), which regulate cravings of drug addiction and memory processes, respectively (Chen et al., 2017). Thus, it is believed that targeting the CB2 receptor and CB2 structure-based design offer promising avenues of new drug discovery

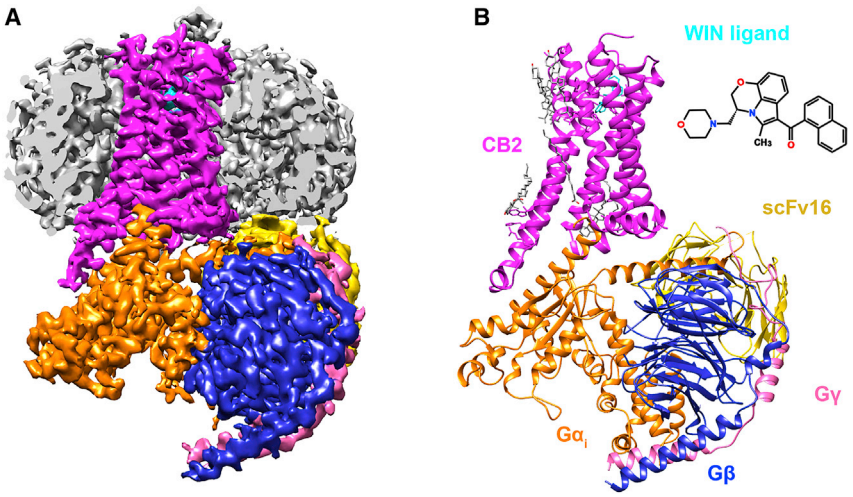

Figure 1. Cryo-EM Structure of CB2-G_i Coupling in Complex with WIN 55,212-2

(A) Cut-through view of the cryo-EM density map of the CB2-WIN 55,212-2-G_i-scFv16 complex. The unsharpened cryo-EM density map at 0.015 contour level, shown as a light gray surface, indicates a micelle. The colored complex cryo-EM density map is shown at 0.022 contour level.

(B) Cartoon representation of CB2-G_i in complex with the antibody scFv16 is shown, with lipids in gray stick representation. Magenta, CB2; cyan, WIN-55,212-2; orange, $G\alpha_i$; blue, Gβ; pink, Gγ; gold, scFv16.

for treatment of a number of disorders while avoiding the severe psychiatric side effects associated with CB1 (Seely et al., 2011).

Activated CB2 mainly couples to the $G_{i/o}$ family and induces $G_{i/o}$-mediated signaling pathways, although $G_{q/11}$ coupling has also been reported (Ibsen et al., 2017). CB2 antagonists and inverse agonists have been reported to promote osteoclast apoptosis and prevent bone loss (Idris et al., 2005). On the other hand, a large body of evidence has indicated a broad therapeutic application of CB2 agonists in neurodegenerative disorders (Aso and Ferrer, 2016; Gómez-Gálvez et al., 2016), drug abuse or addiction (Chen et al., 2017), cardiovascular diseases (Fulmer and Thewke, 2018), and neuroinflammation and neuropathic pain (Lisboa et al., 2018; Turcotte et al., 2016; Guindon and Hohmann, 2008). However, lack of a well-defined CB2 ligand activation and signaling mechanism has hindered development of synthetic CB2 agonists.

WIN 55,212-2 ((R)-(+)-[2,3-dihydro-5-methyl-3-(4-morpholinylmethyl)pyrrolo[1,2,3-de]-1,4-benzoxazin-6-yl]-1-naphthalenylmethanone) is a representative agonist of the cannabinoid receptors CB1 and CB2 (K_i = 62.3 nM and 3.3 nM, respectively), and it has been used extensively to investigate cannabinoid receptor function. In animal models, WIN 55,212-2 has demonstrated efficacy in treating several disease states, including pain (Mohammadi Vosough et al., 2019), seizures (Citraro et al., 2016), and cancer (Roberto et al., 2019). Unlike most CB1 and CB2 agonists, WIN 55,212-2 activates G protein signaling pathways without eliciting CB2 internalization, a property that putatively avoids drug tolerance development. Here we report a 3.2-Å cryoelectron microscopy (cryo-EM) structure of human CB2 bound to the potent agonist WIN 55,212-2 in complex with G_i. Analyses of the ligand binding pocket, the CB2-G_i signaling complex, and conformational dynamics of activated CB2 are conducted by comparisons and contrasts with previously reported structures of inverse agonist-bound CB2 and inverse agonist or agonist-bound CB1. We developed and applied an innovative residual energy calculation algorithm to aid in the design of a pair of selective CB2 agonist and inverse agonist to validate our putative mechanism of receptor activation involving the structural arrangement of critical residues. Our results provide insightful information to facilitate structure-based design and discovery of high-affinity and/or high-selectivity CB2 ligands that can be developed as CB2-targeting therapeutic agents.

RESULTS

Cryo-EM Structure of the CB2-WIN 55,212-2-G_i-scFv16 Complex

To obtain a stable complex of CB2 bound to WIN 55,212-2 and G_i, we co-expressed human CB2 with heterotrimeric G_i protein in insect cells (Figure S1). The receptor-G_i complexes were assembled on the membrane by incubation with WIN 55,212-2 and apyrase. In addition, the antibody fragment scFv16 was added to stabilize the nucleotide-free G_i complex by binding to the interface between $G\alpha_i$ and Gβ (Maeda et al., 2018). The CB2-WIN 55,212-2-G_i-scFv16 complex was then purified through sequential steps of affinity chromatography to homogeneity, yielding a relatively thermostable complex suitable for single-particle cryo-EM analysis (Figure S1).

The structure of the CB2-WIN 55,212-2-G_i-scFv16 complex (Figure 1) was determined from 772,000 particles to a nominal resolution of 3.2 Å (Figure S2), which allowed unambiguous assignment of the transmembrane domain (TMD) of CB2, G_i protein, as well as the antibody fragment in the EM density maps (Figure S3). The α-helical domain (AHD) of $G\alpha_i$, which is poorly resolved in most cryo-EM GPCR-G protein complex structures, is resolved in our CB2-G_i complex structure with a relatively low resolution compared with that of the core structure of this complex. The overall structures were built by rigid body fit of an online homology building model (Kelley et al., 2015). Apart from the AHD of the G_i protein, the majority of the amino acid side chains were well resolved in the final models against the EM density map with excellent geometry (Table S1).

WIN 55,212-2 Interactions in the CB2 Ligand-Binding Pocket

The EM density map shows the binding mode of the CB2 agonist WIN 55,212-2 in the orthosteric binding site in the TMD of CB2.

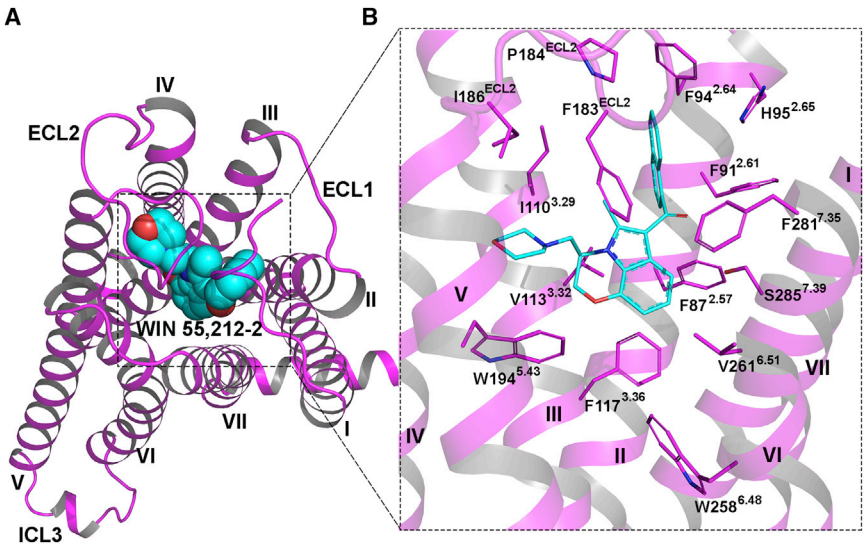

Figure 2. WIN 55,212-2 Binding in the CB2 Orthosteric Ligand-Binding Site

(A) Overview of CB2 in complex with WIN 55,212-2. Cyan sphere model, chemical structure of WIN 55,212-2; magenta cartoon, cryo-EM structure of CB2.

(B) Detailed interactions of WIN 55,212-2 (cyan) within CB2 (magenta). The residues involved in the binding pocket of CB2 are mainly hydrophobic (magenta sticks) and are derived from TM2–TM3, TM5–TM7, and ECL2.

The orientation of the agonist was determined with the electron density and the chemical and geometric constraints of the binding pocket of CB2 (Figure 2). To further validate the binding pose of WIN 55,212-2 in the ligand-binding pocket of CB2, we conducted molecular docking (Figure S4A) using three different software packages or algorithms: Schrödinger-Glide, Auto Dock, and SYBYL-Surflex Dock. The pose of WIN 55,212-2 depicted in our complex structure (Figure S4A) was scored as the top one or two from all three algorithms with the lowest binding energies. We also performed a molecular dynamics simulation, and the results showed that the pose of WIN 55,212-2 in the orthosteric ligand-binding pocket of CB2 is stable (Figures S4B–S4D). The binding interface between WIN 55,212-2 and CB2 is also supported by previously reported mutagenesis-based and structural studies (Li et al., 2019; Zhang et al., 2011; McAllister et al., 2004; Singh et al., 2002).

As shown in Figure 2, the binding pocket of WIN 55,212-2, buried in the transmembrane (TM) region, is formed by residues from TM2–TM3 and TM5–TM7 and capped by extracellular loop 2 (ECL2). The naphthalene moiety of WIN 55,212-2 extends between TM2 and TM3 and is predicted to form strong π-π interactions with $F91^{2.61}$ and $F94^{2.64}$ and hydrophobic interactions with $F87^{2.57}$, $H95^{2.65}$, $P184^{ECL2}$, and $F281^{7.35}$. These results are consistent with the findings from Li et al. (2019), who reported that $F87^{2.57}$, $F91^{2.61}$, $F94^{2.64}$, and $H95^{2.65}$ in TM2 are important for recognition of the CB2 antagonist AM10257. Furthermore, our cryo-EM data reveal that the core structure of WIN 55,212-2 (2,3-dihydro-[1,4]oxazino[2,3,4-*hi*]indole) points downward and engages in π-π interactions with $F117^{3.36}$ and $W258^{6.48}$. It also interacts with $I110^{3.29}$, $V113^{3.32}$, $F183^{ECL2}$, $V261^{6.51}$, and $M265^{6.55}$ via hydrophobic interactions, which have been shown previously to play key roles in ligand binding of CB2. The morpholine moiety of WIN 55,212-2, which adopts the chair conformation, approaches TM5 and ECL2 to form additional hydrophobic interactions with critical residues that have been reported to function in ligand binding (Feng et al., 2014), including $F183^{ECL2}$, $I186^{ECL2}$, and $W194^{5.43}$.

CB2 Activation Mechanism

WIN 55,212-2 has a certain similarity to the antagonist AM10257 in binding to the receptor, but noteworthy differences also exist. From the structural alignment shown in Figure 3A, we may infer that AM10257 (antagonist) and WIN 55,212-2 (agonist) share a similar binding pocket and that most of the interactions with the receptor are conserved (Figure 3A). In addition, the volume of the WIN 55,212-2 binding site within active CB2 (~415 $Å^3$) is similar to that of the AM10257 binding site (antagonist, ~447 $Å^3$). One significant difference is that AM10257 (antagonist; Figure 3A, orange sticks) inserts deeper (2.8 Å) into the binding pocket compared with WIN 55,212-2 (agonist; Figure 3A, cyan sticks), which results in different conformations of the toggle switch residue $W258^{6.48}$. $W258^{6.48}$ is a highly conserved residue in class A GPCRs and has been reported to have a crucial role in GPCR activation (Lin and Sakmar, 1996). In comparison with the inactive CB2, our data showed that $W258^{6.48}$ undergoes a 64° clockwise rotation and $F117^{3.36}$ a 10° counterclockwise rotation in the active CB2 (Figures 3A and 3B). We also noted that the distance between $W258^{6.48}$ and WIN 55,212-2 is about 5.0 Å, greater than that observed for AM10257 (~3.8 Å). Therefore, the steric effects of CB2 ligands on $W258^{6.48}$ appear to play critical roles in determining ligand efficacy.

To further explore the role of critical residues on CB2 activation, we calculated the individual residue energy contribution to determine how much certain residues contribute to the binding of WIN 55,212-2. Briefly, the total binding energy of WIN 55,212-2 at CB2 is the sum of intra-ligand free energy (the energy of WIN 55,212-2) and inter-ligand free energy (the energy between WIN 55,212-2 and residues in CB2), with the latter component further divided into energy contributions from each residue. We quantitatively calculated and compared the residual energy contributions between the inactive and active CB2. Although most of the residues contribute equally to recognition of both antagonist-AM10257 (Figure 3C, green bars) and agonist-WIN 55,212-2 (Figure 3C, magenta bars), three residues, $W194^{5.43}$, $F117^{3.36}$, and $W258^{6.48}$, were found to potentially play important roles in distinguishing agonist from antagonist. This occurs in a manner not requiring direct interaction because they are too far from the WIN 55,212-2 molecule to significantly contribute to its recognition as an agonist (Figure 3C). Several mutagenesis studies from our group and others (Zhang et al., 2011; McAllister

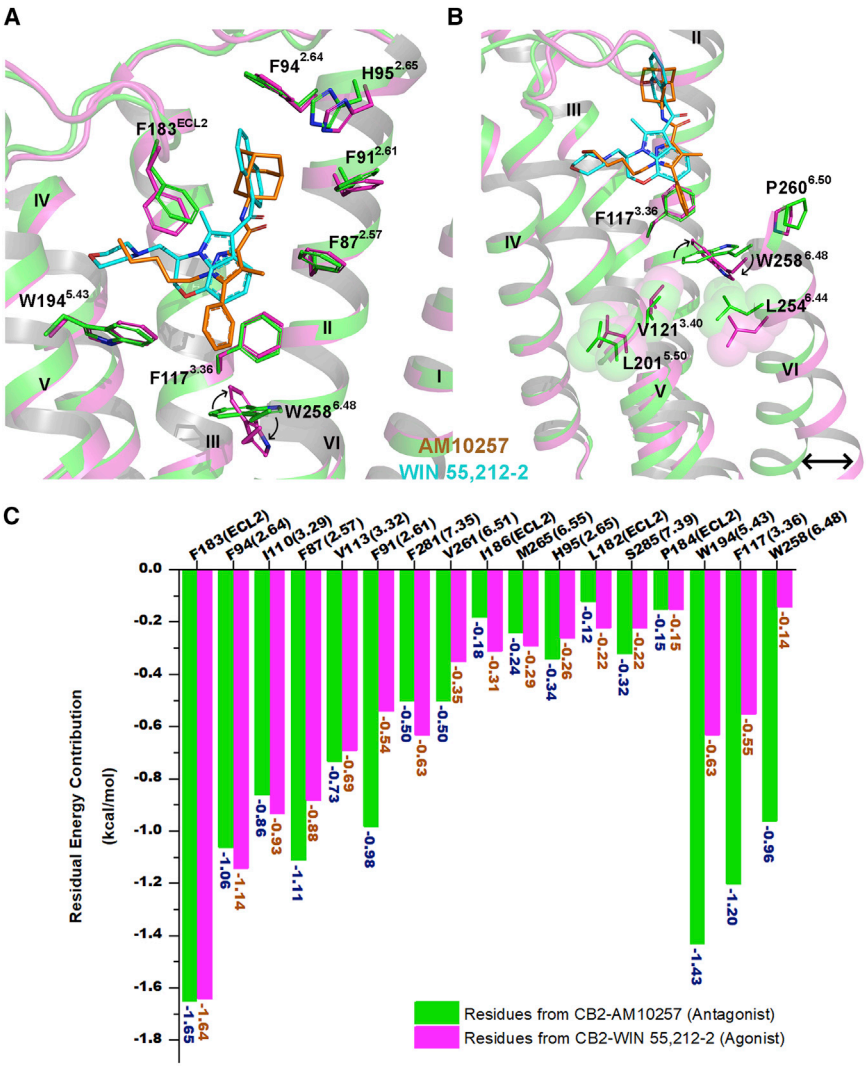

Figure 3. CB2 Activation by WIN 55,212-2

(A) Superposition of the WIN 55,212-2 (cyan)-activated CB2 (magenta) complex with the antagonist (AM10257, orange)-bound CB2 receptor (green) (PDB: 5ZTY; resolution, 2.8 Å).

(B) WIN 55,212-2 bound at the CB2 orthosteric pocket makes direct contact with residues $F117^{3.36}$ and $W258^{6.48}$. The subtle rotation of $F117^{3.36}$ to interact with the 2,3-dihydro-[1,4]oxazino[2,3,4-*hi*]indole moiety of WIN 55,212-2 allows $W258^{6.48}$ to undergo a large rotation with a consequent outward movement of the cytoplasmic end of TM6 that serves to create a cavity for G protein binding. Green cartoon, the inactive CB2 crystal structure (PDB: 5ZTY; resolution, 2.8 Å); magenta cartoon, the active CB2 cryo-EM structure. There is relatively little rearrangement in residues $V121^{3.40}$, $L201^{5.50}$, and $L254^{6.44}$, different from the corresponding residue $Pro^{5.50}$ of β_2AR and μOR, which is involved in packing interactions with $Ile^{3.40}$ and $Phe^{6.44}$ during activation of these GPCRs.

(C) The energy contribution of key residues involved in the binding pockets of inactive and active CB2. Green bars, calculated energy contributions of key residues based on the inactive CB2 crystal structure (PDB: 5ZTY); magenta bars, calculated energy contributions of key residues using the active CB2 cryo-EM structure.

et al., 2004; Singh et al., 2002) also provided evidence of the importance of these three residues in terms of WIN 55,212-2 binding and CB2 activation, further validating our residual energy contribution algorithm. This derivation aids in predicting how to design a functional agonist/antagonist pair based on 3D structure.

To further investigate and validate the structural findings, we rationally designed and synthesized two structurally related CB2-selective compounds and also measured the binding affinity K_i to CB1 and CB2, XIE55 (CB2 K_i = 138 nM, CB1/CB2 > 1,000) and XIE57 (CB2 K_i = 639 nM, CB1/CB2 > 1,000). They share the same pharmacophore but with different chemical moieties; XIE55 has a phenylethylene group, whereas XIE57 has a thiophene ring (Figure 4A; Figure S5). Congruently, cyclic AMP (cAMP) functional assays determined that XIE55 behaves as an inverse agonist and XIE57 acts as a partial agonist of CB2. Molecular docking also showed that these two ligands adopt similar binding poses to interact with CB2 (Figure 4C). The most different feature is that the agonist XIE57 does not extend sufficiently deep to constrain the conformation of $W258^{6.48}$ with a distance of 5.5 Å, whereas the inverse agonist XIE55 approaches closer to $W258^{6.48}$ to form potentially strong π-π interactions (3.0 Å), which is consistent with our structural analysis of the action of WIN 55,212-2 and AM10257, addressed above. This pair of small molecules (XIE55 and XIE57) serves as a "proof of concept" of our method and investigation that can be applied by other researchers in the field for design and discovery of CB2 functional ligands.

Differences between CB2 and CB1

To explore the differences in receptor activation between CB2 and CB1, we aligned the agonist-bound CB2-G_i and agonist-bound CB1-G_i complexes. Although the two ligands, WIN 55,212-2 and Methyl (S)-2-(1-(4-fluorobenzyl)-1H-indazole-3-carboxamido)-3,3-dimethylbutanoate (MDMB)-Fubinaca (FUB), overlap very well, the critical "toggle switch" residues $W^{6.48}$ and $F^{3.36}$ show differences. Specifically, $W356^{6.48}$ in CB1 is positioned about 2.3 Å up toward the extracellular surface, and $F200^{3.36}$ in CB1 is rotated 68° compared with the analogous residues in CB2 (Figure 5A). As a result, the distance between $W356^{6.48}$ and $F200^{3.36}$ in CB1 (4.8 Å) is longer than that in CB2 (3.4 Å). Similarly, the different arrangement of the toggle switch causes a 74° counterclockwise rotation of $F202^{5.51}$ in TM5 of CB2 in comparison with the corresponding residue $L287^{5.51}$ in CB1. Other residues involved in orthosteric binding in CB

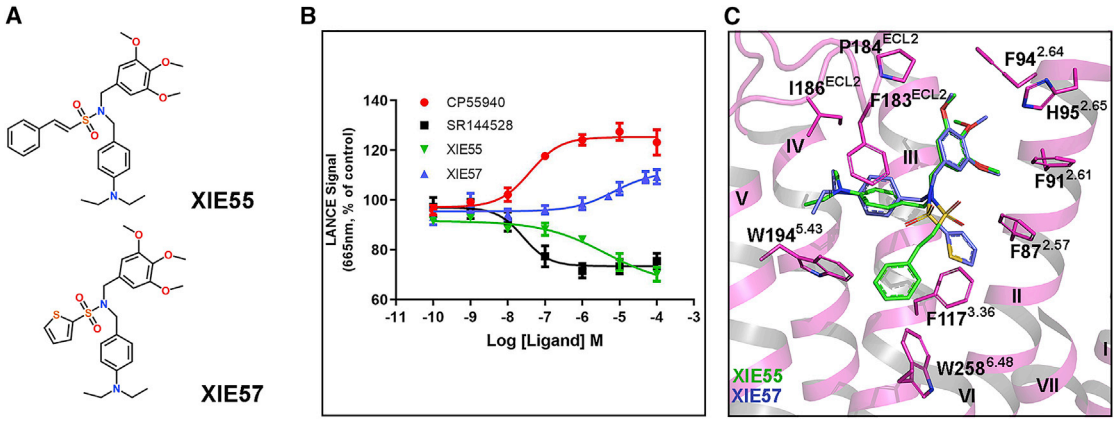

Figure 4. Pharmacology and Molecular Docking of the Designed CB2 Agonist and Antagonist

(A) Chemical structures of the rationally designed antagonist XIE55 and agonist XIE57.

(B) XIE57 acts as a CB2 agonist, whereas XIE55 behaves as a CB2 antagonist, as determined by cAMP assay. The dose-response curves for CP55940, a known agonist, and SR144528, a known inverse agonist, are also shown. CP55940 half maximal effective concentration (EC_{50}), 45.5 ± 24 nM; CP55940 K_i, 1–2 nM; SR144528 EC_{50}, 10.5 ± 4.5 nM; SR144528 K_i, 0.6 nM; XIE57 EC_{50}, 6.9 ± 2.9 μM; XIE57 K_i, 639 nM; XIE55 EC_{50}, 1.5 ± 0.4 μM; XIE55 K_i, 138 nM. Data are presented as mean ± SEM of at least 3 experiments performed in duplicate.

(C) Docking of XIE55 and XIE57 in the WIN 55,212-2-bound CB2 structure (WIN 55,212-2 is removed).

receptors, especially those from TM2 and ECL2, show some conformational differences as well (Figure 5A). Interestingly, the conformation and position of ECLs remain largely unchanged during receptor activation, which can likely be attributed to the C174-C179 disulfide bond and a rigid motif of "PXP" (P176 and P178). We also observed modest upward shifts of residues on the cytoplasmic ends of TM5 and TM6 of CB2 relative to those of CB1 (Figure 5B), which leads to a shift of $Y^{7.53}$ in the NPXXY motif away from $Y^{5.58}$ and $L^{6.41}$ in CB2 compared with that in CB1. Such structural differences in the ligand-binding pockets are associated with observed differences in the conformation of TM5 and TM6 and the G_i coupling interface between CB1 and CB2, indicating that the activation mechanisms of CB1 and CB2 are not the same. All of these structural alterations may be also associated with the distinct interactions of G proteins between CB1 and CB2 (discussed below).

To compare the selectivity between CB2 and CB1, we conducted molecular docking studies and calculated the residual energy contribution for GW-405,833 (L-768,242) on active CB2 and inactive CB1 (PDB: 5TGZ) (Hua et al., 2016). GW-405,833, a dual-function compound (Dhopeshwarkar et al., 2017), acts as a highly selective partial agonist on CB2 (K_i = 3.92 ± 1.58 nM) but as an antagonist on CB1 (K_i = 4772 ± 1,676 nM). The docking poses of GW-405,833 on these two receptors are quite different, as shown in Figure 6A. Moreover, the binding energy of GW-405,833 on CB2 (−10.83 kcal/mol) is greater than that on CB1 (−6.66 kcal/mol), which is consistent with the reported binding affinities for CB2 and CB1. Sequentially, the residual energy contributions for GW-405,833 binding on both CB2 and CB1 were calculated and compared (Figure 6B). Several residues on inactive CB1, including P102 (N terminus), M103 (N terminus), I105 (N terminus), $F170^{2.57}$, and $W356^{6.48}$, are important for GW-405,833 binding. In particular, $W356^{6.48}$ on CB1 contributes greatly (−0.94 kcal/mol) to recognition of GW-405,833 as an antagonist. However, the energy contribution of the corresponding residue $W258^{6.48}$ on CB2 for the partial agonist GW-405,833 is −0.15 kcal/mol (Figure 6B), which is similar to that for WIN 55,212-2. Importantly, $L182^{ECL2}$, $F183^{ECL2}$, $P184^{ECL2}$, and $I186^{ECL2}$ from ECL2 show greater contributions to binding of GW-405,833 on CB2 than the corresponding residues on CB1 (Figure 6B), supporting findings from previous studies (Raitio et al., 2005).

CB2-G_i Coupling and G Protein Selectivity

The overall cryo-EM structure of the CB2-G_i complex reveals a similar interaction mode between the receptor and G protein compared with other G_i or G_s-coupled receptors (Figure S6). The C-terminal α5 helix of the $G\alpha_i$ subunit inserts into the cavity at the cytoplasmic site of CB2 to form the major interaction interface with residues from TM2, ICL2, TM3, TM5, and TM6 of the receptor. When aligned with the reported μ-opioid receptor (μOR)-G_i (PDB: 6DDE) and β_2-adrenergic receptor (β_2AR)-G_s (PDB: 3SN6) complexes (Rasmussen et al., 2011), the α5 helix in CB2-G_i is rotated by 18° and 14°, respectively, along the axis of the membrane (Figures S6A and 6B). However, several striking differences in G_i protein coupling between CB2 and CB1 can be observed. For example, the N terminus of the α5 helix of $G\alpha_i$ in CB2-G_i is closer to TM5 (Figure 7A) and inserts deeper into the receptor binding cavity than those in Rhodopsin-G_i (PDB: 6CMO; Kang et al., 2018) and CB1-G_i (PDB: 6N4B; Li et al., 2019) complexes, as pointed out above. As a result, CB2 forms a more extensive hydrogen-bonding network with the α5 helix of $G\alpha_i$ than that found in the structure of CB1-G_i (Figures 7B and 7C). Specifically, compared with the five hydrophilic interactions between CB1 and $G\alpha_i$ (Li et al., 2019), eight pairs of hydrogen bonds can be observed between CB2 and the α5 helix (Figure 7B). $K67^{2.37}$ and $S69^{2.39}$ in the intracellular side of TM2 are observed to form hydrogen bonds with D350 and C351 in the α5 helix, respectively. $K142^{ICL2}$ in ICL2 interacts with both N347 and D350 via strong hydrogen

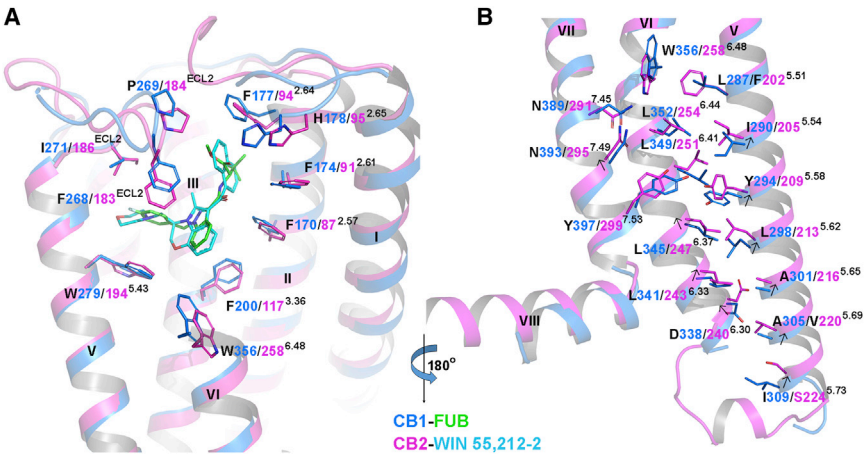

Figure 5. Structure Difference between Agonist-Bound CB2 and Agonist-Bound CB1

(A) A comparison of binding pockets between CB1-G_i and CB2-G_i complexes. Marine cartoon, CB1 structure (PDB: 6N4B; resolution, 3.0 Å); magenta cartoon, CB2 structure; green sticks, FUB; cyan sticks, WIN 55,212-2.

(B) Residue arrangements in the cytoplasmic end of TM5, TM6, and TM7 between the CB1-G_i and CB2-G_i structures. Marine cartoon, CB1 structure (PDB: 6N4B; resolution, 3.0 Å); purple cartoon, CB2 structure. Arrows indicate the movements of residues from CB1 to CB2.

bond interactions. $R131^{3.50}$, a residue of the "ionic lock" in TM3, also forms a hydrogen bond with C351. In addition, $H219^{5.68}$ and $H226^{5.75}$ in TM5 approach D341 and D337 in α5 to form two hydrogen bonds. Finally, we also observed a hydrogen bond between $R242^{6.32}$ and F354. In contrast to CB1, ICL3 in CB2 is well structured and directly interacts with G_i. As shown in Figure 7D, an additional α-helix is formed by residues from ICL3 and TM6, including $R229^{ICL3}$, $Q230^{ICL3}$, $V231^{6.21}$, and $P232^{6.22}$. Two polar residues from ICL3, $Q227^{ICL3}$ and $R229^{ICL3}$, form additional hydrogen bonds with Q304 and E297 of $G\alpha_i$, which are absent in the CB1-G_i complex (Figure S7).

Although CB1 and μOR primarily signal through the $G_{i/o}$ family, previous studies suggested that they can also couple to G_s (Krishna Kumar et al., 2019). However, CB2 does not couple to the G_s family. On the other hand, ICL2 point mutations P139F, P139M, or P139L allow CB2 to couple to G_s in a cAMP-responsive element (CRE)-driven luciferase assay (Zheng et al., 2013). Moreover, a CB2 P139L mutant could activate extracellular signal-regulated kinases (ERK) through both G_i- and G_s-mediated pathways (Zheng et al., 2013). Interestingly, when L222 of CB1 (corresponding to P139 of CB2) is mutated to proline, G_s coupling is lost, but coupling to G_i is retained (Timossi et al., 2002). These studies, together with previous cross-linking studies (Mnpotra et al., 2014), suggest an important role of $P139^{ICL2}$ in G protein selectivity and coupling for CB2.

In our cryo-EM structure, $P139^{ICL2}$ in CB2 interacts with L194 in the β2-β3 loop of G_i but is away from the hydrophobic pocket formed by L194, I343, T340, and F336 in G_i (Figure 7E). It has been suggested that, for CB1, the corresponding residue of $P139^{ICL2}$ in CB2, $L222^{ICL2}$ (Figure 7F), may engage a similar

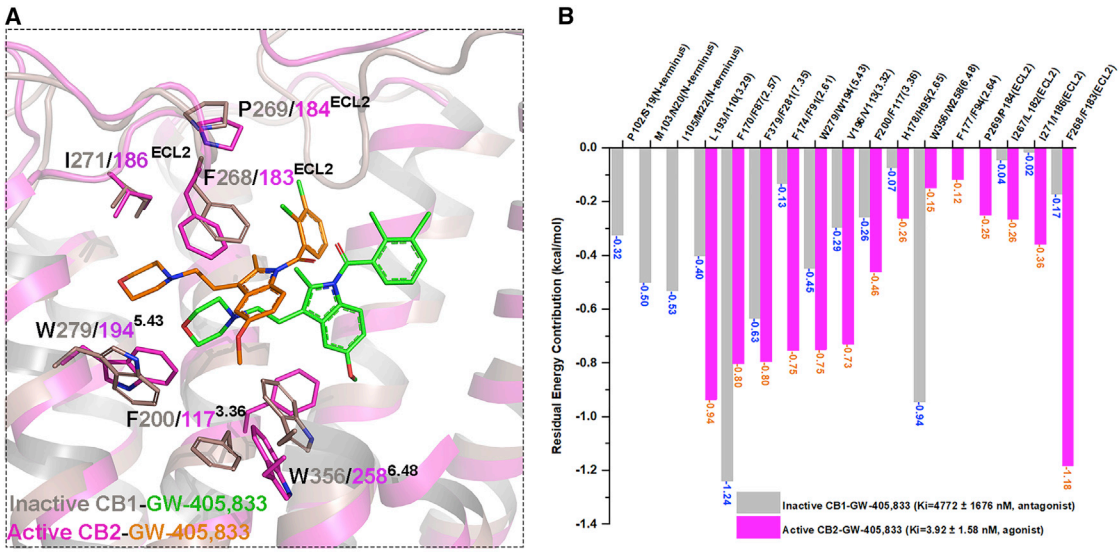

Figure 6. Comparison of Docking Results of the CB2 Selective Partial Agonist GW-405,833 (L-768,242) on Active CB2 and Inactive CB1

(A) Comparison of docking poses and detailed interactions of the CB2-selective partial agonist GW-405,833 on active CB2 (magenta) and inactive CB1 (gray; PDB: 5TGZ). It has been reported that GW-405,833 acts as CB2 agonist (K_i = 3.92 ± 1.58 nM) and CB1 antagonist (K_i = 4,772 ± 1,676 nM).

(B) Comparison of residual energy contribution on GW-405,833 between active CB2 (magenta bars) and inactive CB1 conformations (gray bars).

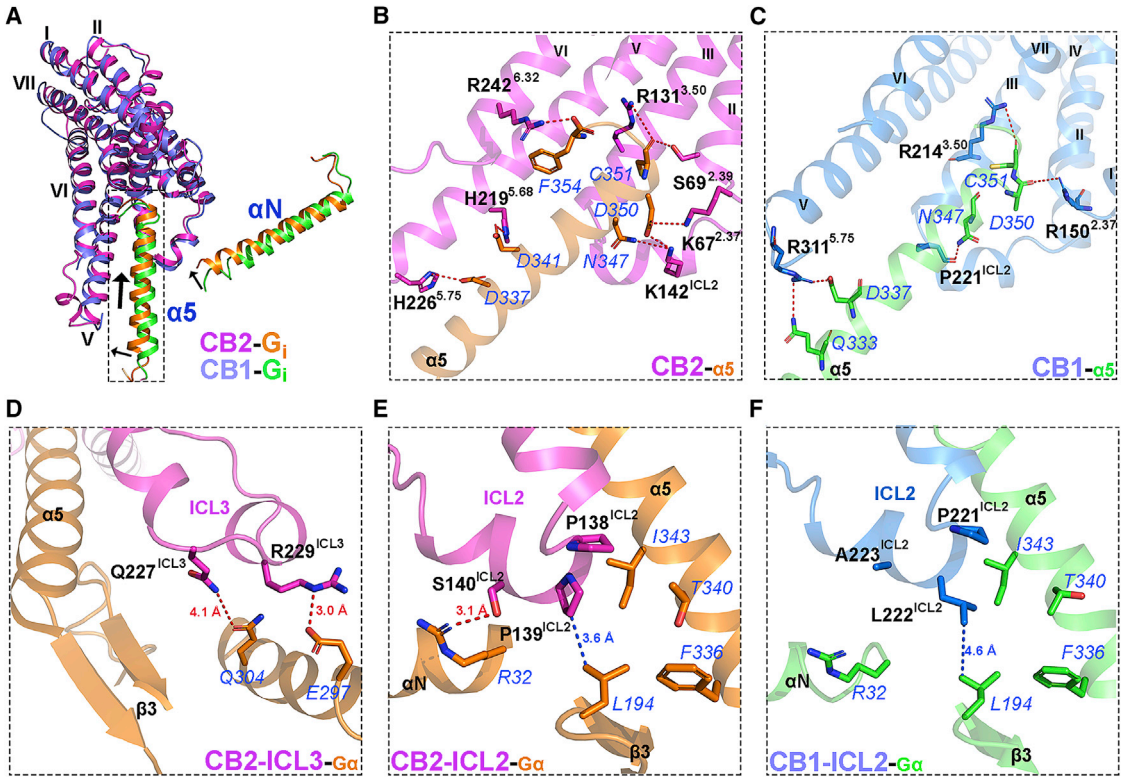

Figure 7. Comparison of the Interface between CB2 and Gα as Well as CB1 and Gα

(A) Overlay of CB2 or CB1 and G_i-α5 structures. Marine cartoon, CB1 structure (PDB: 6N4B; resolution, 3.0 Å); purple cartoon, CB2 structure; orange, G_i-α5/G_i-αN protein of CB2; green, G_i-α5/G_i-αN protein of CB1.

(B) The hydrogen bond network in the complex of CB2-Gα. Magenta cartoon, CB2 structure; orange, Gα protein. Residues from α5 are shown in blue font. The residues belonging to CB2 are shown in black font.

(C) The hydrogen bond network in the complex of CB1-Gα. Marine cartoon, CB1 structure (PDB: 6N4B; resolution, 3.0 Å); green, Gα protein; residues from α5 are shown in blue font. The residues belonging to CB1 are shown in black font.

(D) Detailed interactions between ICL3 of CB2 and Gα. Magenta cartoon, CB2 structure; orange, Gα protein. The hydrogen bonds are indicated by red dashed lines.

(E) Interactions between ICL2 of CB2 and Gα. Magenta cartoon, CB2 structure; orange, Gα protein. The hydrogen bond is indicated by a red dashed line. The hydrophobic interaction is represented by a blue dashed line.

(F) Interactions between ICL2 of CB1 and Gα. Marine cartoon, CB1 structure; green, Gα protein. The hydrophobic interaction is represented by a blue dashed line.

hydrophobic pocket when coupled to G_s, which is important for G_s recognition (Krishna Kumar et al., 2019). However, the $P139^{ICL2}$ in CB2 may not permit interactions with the hydrophobic pocket in G_s because of the rigid "$P138^{ICL2}P139^{ICL2}$" motif, leading to high selectivity of CB2 for G_i over G_s. Consistently, mutation of CB2 $P139^{ICL2}$ to bulkier residues, such as Phe or Leu, might allow such coupling interactions with G_s to be regained.

DISCUSSION

Delineating the CB2 structural basis for ligand recognition and G protein recruitment will facilitate rational design and development of drugs with high affinity and selectivity as well as optimal therapeutic effects. Here we report the cryo-EM structure of an agonist-bound CB2-G_i signaling complex and detailed interactions between the potent agonist WIN 55,212-2 and the receptor, the key residues determining ligand selectivity and efficacy, the differences in activation mechanisms between CB2 and CB1, and the unique molecular features of the CB2-G_i protein interaction. A video of the 3D protein structure can be found at https://youtu.be/x8ucDtoLJi0 for an illustration (the video was not part of the peer review process).

Our 3D cryo-EM structure of CB2 reveals that WIN 55,212-2 occupies the same orthosteric binding pocket as the antagonist AM10257 in CB2 and that it stabilizes the CB2-G_i complex in its active conformation through interference with the toggle switch residue $W258^{6.48}$, which is critical for distinguishing agonists from antagonists. ECL2 and residues from TM2, TM3, and TM6 play important roles in CB2 ligand recognition and ligand selectivity. This provides an advanced strategy for rational design of CB2-selective agonists. The divergent conformation of $W^{6.48}$ in CB1 versus CB2 is associated with a series of distinct residue rearrangements in the intracellular side of TM5, TM6, and TM7 of CB2, as addressed above, which distinguish the activation and G_i signaling mechanism of CB2 from that of CB1. Although several synthetic CB2-selective agonists, including thiophene-containing compounds, have been reported

recently (Scott et al., 2019; Leleu-Chavain et al., 2019; Netteko-ven et al., 2016; Mugnaini et al., 2019; Mukhopadhyay et al., 2016), few have entered clinical trials, and none have so far been approved by the Food and Drug Administration (FDA). The results presented here are likely to aid in the development of potent and selective CB2 ligands with clinical therapy potential.

Comparison of the CB2-G_i complex with CB1-G_i, Rhodopsin-G_i, μOR-G_i, and β_2AR-G_s complexes reveals certain similar overall interaction profiles for receptor-G protein binding. Although CB2 and CB1 share great structural similarity, their interactions with the α5 helix of the G protein remain distinct, reflecting the versatility of G_i coupling. $P139^{ICL2}$ in CB2 and the homologous residue in other GPCRs are critical for G protein coupling, and the unique motif of $P138^{ICL2}P139^{ICL2}$ in ICL2 of CB2 contributes to its G_i coupling specificity. The well-resolved ICL3 structure provides detailed information relating to CB2 interaction with G protein. Our findings, along with the published CB1 structures and CB2 inactive structures, fulfill the complete profile of cannabinoid system receptors and should aid in the rational design of drugs targeting CB2.

STAR★METHODS

Detailed methods are provided in the online version of this paper and include the following:

- KEY RESOURCES TABLE
- LEAD CONTACT AND MATERIALS AVAILABILITY
- EXPERIMENTAL MODEL AND SUBJECT DETAILS
  - Cell lines
- METHOD DETAILS
  - Constructs
  - Protein complex expression, formation, and purification
  - Sample preparation and EM data collection
  - Image processing and 3-D reconstructions
  - Model building and refinement
  - Protein thermostability assay
  - Synthesis and characterization of XIE55 and XIE57
  - (E)-N-(4-(diethylamino)benzyl)-2-phenyl-N-(3,4,5-trimethoxybenzyl)ethene-1-sulfonamide (XIE55)
  - N-(4-(diethylamino)benzyl)-N-(3,4,5-trimethoxybenzyl) thiophene-2-sulfonamide (XIE57)
  - CB2 radioligand competition binding assay
  - cAMP functional assay
  - Quantitative characterization of binding residues on CB2
  - Molecular docking
  - MD simulations
  - Figure preparation
- QUANTIFICATION AND STATISTICAL ANALYSIS
- DATA AND CODE AVAILABILITY

SUPPLEMENTAL INFORMATION

Supplemental Information can be found online at https://doi.org/10.1016/j.cell.2020.01.007.

ACKNOWLEDGMENTS

The project is supported by funding to the Xie Laboratory and Center from the National Institutes of Health (NIH) National Institute on Drug Abuse (NIDA) (P30 DA035778A1) and NIH (R01 DA025612) (to X.-Q.X.), NIH grants 1R35GM128641 (to C.Z.) and 1R01GM127710 (to H.E.X.), the Jay and Betty Van Andel Foundation (to H.E.X.), and the Ministry of Science and Technology of China (XDB08020303) (to H.E.X.). The cryo-EM data were collected at the David Van Andel Advanced Cryo-Electron Microscopy Suite at the Van Andel Research Institute. Y.Z. was supported by the UCAS Joint PhD Training Program.

AUTHOR CONTRIBUTIONS

X.-Q.X., H.E.X., C.Z., and Z.F. conceived the project, designed the research, and wrote the paper with contributions from all authors. X.-Q.X. and C.X. initiated the project. C.X. prepared samples with the help of C.Z., H.L., and L.W. C.X. optimized the constructs with the help of Y.Z. Y.Z. optimized the protein sample preparation conditions, conducted the CPM assay, and prepared the final sample for cryo-EM data collection. Y.Z. and T.-H.X. performed data acquisition, image processing, and structure determination under the supervision of H.E.X. and K.M. and prepared the figures and manuscript for writing. C.X. characterized the synthesized ligands and conducted cAMP functional assays, supervised by X.-Q.X. and T.F.M. C.X. prepared figures and wrote the manuscript. Z.F. performed computational experiments, analyzed the structure, prepared figures, and wrote the manuscript. J.W. performed and analyzed the molecular dynamics simulation. M.C. developed the algorithm for protein quantitative characterization and performed the computation. T.F.M., Y.X., K.M., and G.Z. helped significantly with review and editing. X.E.Z. and X.M. provided advice regarding model refinement and data collection.

DECLARATION OF INTERESTS

The authors declare no competing interests.

Received: July 18, 2019
Revised: November 1, 2019
Accepted: January 6, 2020
Published: January 30, 2020

REFERENCES

Adams, P.D., Afonine, P.V., Bunkóczi, G., Chen, V.B., Davis, I.W., Echols, N., Headd, J.J., Hung, L.W., Kapral, G.J., Grosse-Kunstleve, R.W., et al. (2010). PHENIX: a comprehensive Python-based system for macromolecular structure solution. Acta Crystallogr. D Biol. Crystallogr. *66*, 213–221.

Adams, P.D., Afonine, P.V., Bunkóczi, G., Chen, V.B., Echols, N., Headd, J.J., Hung, L.W., Jain, S., Kapral, G.J., Grosse Kunstleve, R.W., McCoy, A.J., Moriarty, N.W., Oeffner, R.D., Read, R.J., Richardson, D.C., Richardson, J.S., Terwilliger, T.C., and Zwart, P.H. (2011). The Phenix software for automated determination of macromolecular structures. Methods *55*, 94–106.

Aronne, L.J., Tonstad, S., Moreno, M., Gantz, I., Erondu, N., Suryawanshi, S., Molony, C., Sieberts, S., Nayee, J., Meehan, A.G., et al. (2010). A clinical trial assessing the safety and efficacy of taranabant, a CB1R inverse agonist, in obese and overweight patients: a high-dose study. Int. J. Obes. *34*, 919–935.

Aso, E., and Ferrer, I. (2016). CB2 cannabinoid receptor as potential target against Alzheimer's disease. Front. Neurosci. *10*, 243.

Calignano, A., La Rana, G., Giuffrida, A., and Piomelli, D. (1998). Control of pain initiation by endogenous cannabinoids. Nature *394*, 277–281.

Case, D.A., Ben-Shalom, I.Y., Brozell, S.R., Cerutti, D.S., Cheatham, T.E., III, Cruzeiro, V.W.D., Darden, T.A., Duke, R.E., Ghoreishi, D., Gilson, M.K., et al. (2018). AMBER 2018 (San Francisco: University of California).

Chen, D.-J., Gao, M., Gao, F.-F., Su, Q.-X., and Wu, J. (2017). Brain cannabinoid receptor 2: expression, function and modulation. Acta Pharmacol. Sin. *38*, 312–316.

Chen, M., Jing, Y., Wang, L., Feng, Z., and Xie, X.-Q. (2019). DAKB-GPCRs: An Integrated Computational Platform for Drug Abuse Related GPCRs. J. Chem. Inf. Model. *59*, 1283–1289.

Citraro, R., Russo, E., Leo, A., Russo, R., Avagliano, C., Navarra, M., Calignano, A., and De Sarro, G. (2016). Pharmacokinetic-pharmacodynamic influence of N-palmitoylethanolamine, arachidonyl-2′-chloroethylamide and WIN 55,212-2 on the anticonvulsant activity of antiepileptic drugs against audiogenic seizures in DBA/2 mice. Eur. J. Pharmacol. *791*, 523–534.

Dhopeshwarkar, A., Murataeva, N., Makriyannis, A., Straiker, A., and Mackie, K. (2017). Two Janus cannabinoids that are both CB2 agonists and CB1 antagonists. J. Pharmacol. Exp. Ther. *360*, 300–311.

Dickson, C.J., Madej, B.D., Skjevik, A.A., Betz, R.M., Teigen, K., Gould, I.R., and Walker, R.C. (2014). Lipid14: The Amber Lipid Force Field. J. Chem. Theory Comput. *10*, 865–879.

Emsley, P., and Cowtan, K. (2004). Coot: model-building tools for molecular graphics. Acta Crystallogr. D Biol. Crystallogr. *60*, 2126–2132.

Feng, Z., Alqarni, M.H., Yang, P., Tong, Q., Chowdhury, A., Wang, L., and Xie, X.-Q. (2014). Modeling, molecular dynamics simulation, and mutation validation for structure of cannabinoid receptor 2 based on known crystal structures of GPCRs. J. Chem. Inf. Model. *54*, 2483–2499.

Feng, Z., Pearce, L.V., Xu, X., Yang, X., Yang, P., Blumberg, P.M., and Xie, X.-Q. (2015). Structural insight into tetrameric hTRPV1 from homology modeling, molecular docking, molecular dynamics simulation, virtual screening, and bioassay validations. J. Chem. Inf. Model. *55*, 572–588.

Fulmer, M.L., and Thewke, D.P. (2018). The Endocannabinoid System and Heart Disease: The Role of Cannabinoid Receptor Type 2. Cardiovasc. Hematol. Disord. Drug Targets *18*, 34–51.

Galiègue, S., Mary, S., Marchand, J., Dussossoy, D., Carrière, D., Carayon, P., Bouaboula, M., Shire, D., Le Fur, G., and Casellas, P. (1995). Expression of central and peripheral cannabinoid receptors in human immune tissues and leukocyte subpopulations. Eur. J. Biochem. *232*, 54–61.

Gómez-Gálvez, Y., Palomo-Garo, C., Fernández-Ruiz, J., and García, C. (2016). Potential of the cannabinoid CB(2) receptor as a pharmacological target against inflammation in Parkinson's disease. Prog. Neuropsychopharmacol. Biol. Psychiatry *64*, 200–208.

Guindon, J., and Hohmann, A.G. (2008). Cannabinoid CB2 receptors: a therapeutic target for the treatment of inflammatory and neuropathic pain. Br. J. Pharmacol. *153*, 319–334.

Hawkins, G.D., Cramer, C.J., and Truhlar, D.G. (1996). Parametrized models of aqueous free energies of solvation based on pairwise descreening of solute atomic charges from a dielectric medium. J. Phys. Chem. *100*, 19824–19839.

Hou, T., Wang, J., Li, Y., and Wang, W. (2011a). Assessing the performance of the MM/PBSA and MM/GBSA methods. 1. The accuracy of binding free energy calculations based on molecular dynamics simulations. J. Chem. Inf. Model. *51*, 69–82.

Hou, T., Wang, J., Li, Y., and Wang, W. (2011b). Assessing the performance of the molecular mechanics/Poisson Boltzmann surface area and molecular mechanics/generalized Born surface area methods. II. The accuracy of ranking poses generated from docking. J. Comput. Chem. *32*, 866–877.

Hua, T., Vemuri, K., Pu, M., Qu, L., Han, G.W., Wu, Y., Zhao, S., Shui, W., Li, S., Korde, A., et al. (2016). Crystal structure of the human cannabinoid receptor CB1. Cell *167*, 750–762.e14.

Ibsen, M.S., Connor, M., and Glass, M. (2017). Cannabinoid CB_1 and CB_2 Receptor Signaling and Bias. Cannabis Cannabinoid Res. *2*, 48–60.

Idris, A.I., and Ralston, S.H. (2012). Role of cannabinoids in the regulation of bone remodeling. Front. Endocrinol. (Lausanne) *3*, 136.

Idris, A.I., van 't Hof, R.J., Greig, I.R., Ridge, S.A., Baker, D., Ross, R.A., and Ralston, S.H. (2005). Regulation of bone mass, bone loss and osteoclast activity by cannabinoid receptors. Nat. Med. *11*, 774–779.

Jorgensen, W.L., Chandrasekhar, J., Madura, J.D., Impey, R.W., and Klein, M.L. (1983). Comparison of simple potential functions for simulating liquid water. J. Chem. Phys. *79*, 926.

Kang, Y., Kuybeda, O., de Waal, P.W., Mukherjee, S., Van Eps, N., Dutka, P., Zhou, X.E., Bartesaghi, A., Erramilli, S., Morizumi, T., et al. (2018). Cryo-EM structure of human rhodopsin bound to an inhibitory G protein. Nature *558*, 553–558.

Kelley, L.A., Mezulis, S., Yates, C.M., Wass, M.N., and Sternberg, M.J. (2015). The Phyre2 web portal for protein modeling, prediction and analysis. Nat. Protoc. *10*, 845–858.

Kirkham, T.C. (2005). Endocannabinoids in the regulation of appetite and body weight. Behav. Pharmacol. *16*, 297–313.

Koehl, A., Hu, H., Maeda, S., Zhang, Y., Qu, Q., Paggi, J.M., Latorraca, N.R., Hilger, D., Dawson, R., Matile, H., and Schertler, G.F. (2018). Structure of the μ-opioid receptor–G i protein complex. Nature *558*, 547–552.

Krishna Kumar, K., Shalev-Benami, M., Robertson, M.J., Hu, H., Banister, S.D., Hollingsworth, S.A., Latorraca, N.R., Kato, H.E., Hilger, D., Maeda, S., et al. (2019). Structure of a Signaling Cannabinoid Receptor 1-G protein complex. Cell *176*, 448–458.e12.

Kucukelbir, A., Sigworth, F.J., and Tagare, H.D. (2014). Quantifying the local resolution of cryo-EM density maps. Nat. Methods *11*, 63–65.

Leleu-Chavain, N., Baudelet, D., Heloire, V.M., Rocha, D.E., Renault, N., Barczyk, A., Djouina, M., Body-Malapel, M., Carato, P., and Millet, R. (2019). Benzo [d]thiazol-2(3H)-ones as new potent selective CB_2 agonists with anti-inflammatory properties. Eur. J. Med. Chem. *165*, 347–362.

Li, X., Hua, T., Vemuri, K., Ho, J.H., Wu, Y., Wu, L., Popov, P., Benchama, O., Zvonok, N., Locke, K., et al. (2019). Crystal Structure of the Human Cannabinoid Receptor CB2. Cell *176*, 459–467.e13.

Li, H., Leung, K.-S., and Wong, M.-H. (2012). idock: A multithreaded virtual screening tool for flexible ligand docking. 2012 IEEE Symposium on Computational Intelligence in Bioinformatics and Computational Biology (CIBCB), pp. 77–84.

Liang, Y.-L., Zhao, P., Draper-Joyce, C., Baltos, J.-A., Glukhova, A., Truong, T.T., May, L.T., Christopoulos, A., Wootten, D., Sexton, P.M., and Furness, S.G.B. (2018). Dominant negative G proteins enhance formation and purification of agonist-GPCR-G protein complexes for structure determination. ACS Pharmacol. Transl. Sci. *1*, 12–20.

Lin, S.W., and Sakmar, T.P. (1996). Specific tryptophan UV-absorbance changes are probes of the transition of rhodopsin to its active state. Biochemistry *35*, 11149–11159.

Lisboa, S.F., Niraula, A., Resstel, L.B., Guimaraes, F.S., Godbout, J.P., and Sheridan, J.F. (2018). Repeated Social Defeat-Induced Neuroinflammation, Anxiety-like behavior and Resistance to Fear Extinction were Attenuated by the Cannabinoid Receptor Agonist WIN55, 212-2. Neuropsychopharmacology *43*, 1924–1933.

Maeda, S., Koehl, A., Matile, H., Hu, H., Hilger, D., Schertler, G.F.X., Manglik, A., Skiniotis, G., Dawson, R.J.P., and Kobilka, B.K. (2018). Development of an antibody fragment that stabilizes GPCR/G-protein complexes. Nat. Commun. *9*, 3712.

Maier, J.A., Martinez, C., Kasavajhala, K., Wickstrom, L., Hauser, K.E., and Simmerling, C. (2015). ff14SB: Improving the Accuracy of Protein Side Chain and Backbone Parameters from ff99SB. J. Chem. Theory Comput. *11*, 3696–3713.

Maroon, J., and Bost, J. (2018). Review of the neurological benefits of phytocannabinoids. Surg. Neurol. Int. *9*, 91.

Mastronarde, D.N. (2005). Automated electron microscope tomography using robust prediction of specimen movements. J. Struct. Biol. *152*, 36–51.

McAllister, S.D., Hurst, D.P., Barnett-Norris, J., Lynch, D., Reggio, P.H., and Abood, M.E. (2004). Structural mimicry in class A G protein-coupled receptor rotamer toggle switches: the importance of the F3.36(201)/W6.48(357) interaction in cannabinoid CB1 receptor activation. J. Biol. Chem. *279*, 48024–48037.

Mnpotra, J.S., Qiao, Z., Cai, J., Lynch, D.L., Grossfield, A., Leioatts, N., Hurst, D.P., Pitman, M.C., Song, Z.H., and Reggio, P.H. (2014). Structural basis of G

protein-coupled receptor-Gi protein interaction: formation of the cannabinoid CB2 receptor-Gi protein complex. J. Biol. Chem. *289*, 20259–20272.

Mohammadi Vosough, E., Baradaran Rahimi, V., Masoud, S.A., Mirkarimi, H.R., Demneh, M.K., Abed, A., Banafshe, H.R., and Askari, V.R. (2019). Evaluation of protective effects of non-selective cannabinoid receptor agonist WIN 55,212-2 against the nitroglycerine-induced acute and chronic animal models of migraine: A mechanistic study. Life Sci. *232*, 16670.

Moreira, F.A., and Crippa, J.A. (2009). The psychiatric side-effects of rimonabant. Br. J. Psychiatry *31*, 145–153.

Mugnaini, C., Rabbito, A., Brizzi, A., Palombi, N., Petrosino, S., Verde, R., Di Marzo, V., Ligresti, A., and Corelli, F. (2019). Synthesis of novel 2-(1-adamantanylcarboxamido)thiophene derivatives. Selective cannabinoid type 2 (CB2) receptor agonists as potential agents for the treatment of skin inflammatory disease. Eur. J. Med. Chem. *161*, 239–251.

Mukhopadhyay, P., Baggelaar, M., Erdelyi, K., Cao, Z., Cinar, R., Fezza, F., Ignatowska-Janlowska, B., Wilkerson, J., van Gils, N., Hansen, T., et al. (2016). The novel, orally available and peripherally restricted selective cannabinoid CB2 receptor agonist LEI-101 prevents cisplatin-induced nephrotoxicity. Br. J. Pharmacol. *173*, 446–458.

Nettekoven, M., Adam, J.M., Bendels, S., Bissantz, C., Fingerle, J., Grether, U., Grüner, S., Guba, W., Kimbara, A., Ottaviani, G., et al. (2016). Novel Triazolopyrimidine-Derived Cannabinoid Receptor 2 Agonists as Potential Treatment for Inflammatory Kidney Diseases. ChemMedChem *11*, 179–189.

Onaivi, E.S., Ishiguro, H., Gong, J.P., Patel, S., Perchuk, A., Meozzi, P.A., Myers, L., Mora, Z., Tagliaferro, P., Gardner, E., et al. (2006). Discovery of the presence and functional expression of cannabinoid CB2 receptors in brain. Ann. N Y Acad. Sci. *1074*, 514–536.

Ouyang, Q., Tong, Q., Feng, R., Myint, K.-Z., Yang, P., and Xie, X.Q. (2013). Trisubstituted Sulfonamides: a New Chemotype for Development of Potent and Selective CB2 Receptor Inverse Agonists. ACS Med. Chem. Lett. *4*, 387–392.

Pettersen, E.F., Goddard, T.D., Huang, C.C., Couch, G.S., Greenblatt, D.M., Meng, E.C., and Ferrin, T.E. (2004). UCSF Chimera--a visualization system for exploratory research and analysis. J. Comput. Chem. *25*, 1605–1612.

Proietto, J., Rissanen, A., Harp, J.B., Erondu, N., Yu, Q., Suryawanshi, S., Jones, M.E., Johnson-Levonas, A.O., Heymsfield, S.B., Kaufman, K.D., and Amatruda, J.M. (2010). A clinical trial assessing the safety and efficacy of the CB1R inverse agonist taranabant in obese and overweight patients: low-dose study. Int. J. Obes. *34*, 1243–1254.

Punjani, A., Rubinstein, J.L., Fleet, D.J., and Brubaker, M.A. (2017). cryoSPARC: algorithms for rapid unsupervised cryo-EM structure determination. Nat. Methods *14*, 290–296.

Raitio, K.H., Salo, O.M., Nevalainen, T., Poso, A., and Järvinen, T. (2005). Targeting the cannabinoid CB2 receptor: mutations, modeling and development of CB2 selective ligands. Curr. Med. Chem. *12*, 1217–1237.

Rasmussen, S.G., DeVree, B.T., Zou, Y., Kruse, A.C., Chung, K.Y., Kobilka, T.S., Thian, F.S., Chae, P.S., Pardon, E., Calinski, D., et al. (2011). Crystal structure of the β2 adrenergic receptor-Gs protein complex. Nature *477*, 549–555.

Roberto, D., Klotz, L.H., and Venkateswaran, V. (2019). Cannabinoid WIN 55,212-2 induces cell cycle arrest and apoptosis, and inhibits proliferation, migration, invasion, and tumor growth in prostate cancer in a cannabinoid-receptor 2 dependent manner. Prostate *79*, 151–159.

Rohou, A., and Grigorieff, N. (2015). CTFFIND4: Fast and accurate defocus estimation from electron micrographs. J. Struct. Biol. *192*, 216–221.

Rosenthal, P.B., and Henderson, R. (2003). Optimal determination of particle orientation, absolute hand, and contrast loss in single-particle electron cryomicroscopy. J. Mol. Biol. *333*, 721–745.

Scott, C.E., Tang, Y., Alt, A., Burford, N.T., Gerritz, S.W., Ogawa, L.M., Zhang, L., and Kendall, D.A. (2019). Identification and biochemical analyses of selective CB_2 agonists. Eur. J. Pharmacol. *854*, 1–8.

Seeley, R.J., and Woods, S.C. (2003). Monitoring of stored and available fuel by the CNS: implications for obesity. Nat. Rev. Neurosci. *4*, 901–909.

Seely, K.A., Prather, P.L., James, L.P., and Moran, J.H. (2011). Marijuana-based drugs: innovative therapeutics or designer drugs of abuse? Mol. Interv. *11*, 36–51.

Singh, R., Hurst, D.P., Barnett-Norris, J., Lynch, D.L., Reggio, P.H., and Guarnieri, F. (2002). Activation of the cannabinoid CB1 receptor may involve a W6 48/F3 36 rotamer toggle switch. J. Pept. Res. *60*, 357–370.

Śledziński, P., Zeyland, J., Słomski, R., and Nowak, A. (2018). The current state and future perspectives of cannabinoids in cancer biology. Cancer Med. *7*, 765–775.

Timossi, C., Maldonado, D., Vizcaíno, A., Lindau-Shepard, B., Conn, P.M., and Ulloa-Aguirre, A. (2002). Structural determinants in the second intracellular loop of the human follicle-stimulating hormone receptor are involved in G(s) protein activation. Mol. Cell. Endocrinol. *189*, 157–168.

Trott, O., and Olson, A.J. (2010). AutoDock Vina: improving the speed and accuracy of docking with a new scoring function, efficient optimization, and multithreading. J. Comput. Chem. *31*, 455–461.

Turcotte, C., Blanchet, M.-R., Laviolette, M., and Flamand, N. (2016). The CB_2 receptor and its role as a regulator of inflammation. Cell. Mol. Life Sci. *73*, 4449–4470.

Walter, L., and Stella, N. (2004). Cannabinoids and neuroinflammation. Br. J. Pharmacol. *141*, 775–785.

Wang, J.M., Hou, T.J., and Xu, X.J. (2006). Recent Advances in Free Energy Calculations with a Combination of Molecular Mechanics and Continuum Models. Curr. Computer-Aided Drug Des. *2*, 287–306.

Wang, J., Wolf, R.M., Caldwell, J.W., Kollman, P.A., and Case, D.A. (2004). Development and testing of a general amber force field. J. Comput. Chem. *25*, 1157–1174.

Williams, C.J., Headd, J.J., Moriarty, N.W., Prisant, M.G., Videau, L.L., Deis, L.N., Verma, V., Keedy, D.A., Hintze, B.J., Chen, V.B., and Jain, S. (2018). MolProbity: More and better reference data for improved all-atom structure validation. Protein Sci. *27*, 293–315.

Yang, P., Myint, K.Z., Tong, Q., Feng, R., Cao, H., Almehizia, A.A., Alqarni, M.H., Wang, L., Bartlow, P., Gao, Y., et al. (2012a). Lead discovery, chemistry optimization, and biological evaluation studies of novel biamide derivatives as CB2 receptor inverse agonists and osteoclast inhibitors. J. Med. Chem. *55*, 9973–9987.

Yang, P., Wang, L., and Xie, X.-Q. (2012b). Latest advances in novel cannabinoid CB(2) ligands for drug abuse and their therapeutic potential. Future Med. Chem. *4*, 187–204.

Yin, J., Chapman, K., Clark, L.D., Shao, Z., Borek, D., Xu, Q., Wang, J., and Rosenbaum, D.M. (2018). Crystal structure of the human NK_1 tachykinin receptor. Proc. Natl. Acad. Sci. USA *115*, 13264–13269.

Zhang, Y., Xie, Z., Wang, L., Schreiter, B., Lazo, J.S., Gertsch, J., and Xie, X.Q. (2011). Mutagenesis and computer modeling studies of a GPCR conserved residue W5.43(194) in ligand recognition and signal transduction for CB2 receptor. Int. Immunopharmacol. *11*, 1303–1310.

Zheng, C., Chen, L., Chen, X., He, X., Yang, J., Shi, Y., and Zhou, N. (2013). The second intracellular loop of the human cannabinoid CB2 receptor governs G protein coupling in coordination with the carboxyl terminal domain. PLoS ONE *8*, e63262.

Zheng, S.Q., Palovcak, E., Armache, J.P., Verba, K.A., Cheng, Y., and Agard, D.A. (2017). MotionCor2: anisotropic correction of beam-induced motion for improved cryo-electron microscopy. Nat. Methods *14*, 331–332.

Zivanov, J., Nakane, T., Forsberg, B.O., Kimanius, D., Hagen, W.J., Lindahl, E., and Scheres, S.H. (2018). New tools for automated high-resolution cryo-EM structure determination in RELION-3. eLife *7*, e42166.

STAR★METHODS

KEY RESOURCES TABLE

REAGENT or RESOURCE	SOURCE	IDENTIFIER
Chemicals, Peptides, and Recombinant Proteins		
WIN 55,212-2 Mesylate	MedChemExpress	Cat# HY-13291
(−)-CP 55,940	Cayman Chemical	Cat# 90084
Lauryl maltose neopentyl glycol	Anatrace	Cat# NG310
n-dodecyl-β-D-maltoside (DDM)	Anatrace	Cat# D310S
Cholesteryl Hemisuccinate	Anatrace	Cat# CH210
CHAPS	Fisher Bioreagents	Cat# BP5715
Digitonin	Millipore Sigma	Cat# 30-041-01GM
Leupeptin	Sigma-Aldrich	Cat# L2884
Benzamidine	Sigma-Aldrich	Cat# 12072
FLAG peptide	GL Biochem	Custom Synthesis
GDP	Sigma Aldrich	Cat# G7127
ESF921 culture medium	Expression System	Cat# NC9541308
2-Mercaptoethanol	Sigma-Aldrich	Cat# M6250
Apyrase	New England Biolabs	Cat# M0398L
PNGase F	New England Biolabs	Cat# P0704S
TEV protease	Prepared In-House	N/A
Anti-Flag M1 resin	Sigma Aldrich	Cat# A4596
N-[4-(7-diethylamino-4-methyl-3-coumarinyl)phenyl]maleimide (CPM)	Sigma	Cat#C1484
FuGENE Transfection Reagent	Promega	Cat#E2311
DyLight 488	Thermo Fisher	Cat#46402
Critical Commercial Assays		
LANCE cAMP Detection Kit	PerkinElmer	Cat# AD0262
Deposited Data		
CB2-Gi coordinates	This paper	PDB: 6PT0
CB2-Gi EM map	This paper	EMDB: EMD-20470
Experimental Models: Cell Lines		
Spodoptera frugiperda Sf9 cells	Novagen	Cat# 71104-3
CHO-K1	PerkinElmer	Cat# ES-111-C
Oligonucleotides		
CB2 forward primer	IDT	N/A
CB2 reverse primer	IDT	N/A
Recombinant DNA		
pFastbac-prolactin-Flag-BN-CB2-H8	This paper	N/A
pFastbac-Gαi1_4M	This paper	N/A
pFastbac-H8-Gβ1	This paper	N/A
pFastbac-Gγ2	This paper	N/A
pFastbac-GP67-scFv16-H8	This paper	N/A
Software and Algorithms		
Clonemanager	Sci-Ed Software	http://www.scied.com/pr_cmpro.htm
Prism7	GraphPad	https://www.graphpad.com/scientific-software/prism/
SerialEM	Mastronarde, 2005	http://bio3d.colorado.edu/SerialEM/

(*Continued on next page*)

Continued

REAGENT or RESOURCE	SOURCE	IDENTIFIER
MotionCor2	Zheng et al., 2017	https://msg.ucsf.edu/em/software/motioncor2.html
Relion 3.0	Zivanov et al., 2018	https://www3.mrc-lmb.cam.ac.uk/relion/index.php/Download_%26_install
UCSF Chimera	Pettersen et al., 2004	https://www.cgl.ucsf.edu/chimera/
Phenix	Adams et al., 2011	https://www.phenix-online.org/
Coot	Emsley and Cowtan, 2004	https://www2.mrc-lmb.cam.ac.uk/personal/pemsley/coot/
PyMol 2.3	Schrödinger	https://pymol.org/2/
MolProbity	Williams et al., 2018	http://molprobity.biochem.duke.edu/
Other		
Quantifoil R1.2/1.3 300-mesh holey carbon-coated grids	Quantifoil	https://www.emsdiasum.com/microscopy/products/grids/quantifoil.aspx
Nickel Sepharose resin	GE healthcare	Cat#17526801
Superdex 200 Increase column	GE healthcare	Cat#28990944

LEAD CONTACT AND MATERIALS AVAILABILITY

Further information and requests for resources and reagents should be directed to and will be fulfilled by the Lead Contact, Xiang-Qun Xie (xix15@pitt.edu). All unique/stable reagents generated in this study are available from the Lead Contact with a completed Materials Transfer Agreement.

EXPERIMENTAL MODEL AND SUBJECT DETAILS

Cell lines

Chinese hamster ovary (CHO)-K1 cells (PerkinElmer) were cultured in DMEM/F-12 medium (GIBCO) supplemented with 10% fetal bovine serum at 37°C with 5% CO_2. Spodoptera frugiperda Sf9 cells (Novagen) were cultured in ESF 921 serum-free medium (Expression Systems) in 27°C. CHO-K1 cells overexpressing CB2 were used in radioligand-binding assays and cAMP functional assays. Sf9 cells were used exclusively for recombinant protein expression.

METHOD DETAILS

Constructs

The full-length gene coding sequence of wild-type human CB2 was cloned into pFastBac vector (ThermoFisher) with an N-terminal FLAG tag followed by β2-AR N-terminal tail region (BN, hereafter) as fusion protein and a TEV cleavage site, along with a His8 tag at the C-terminal to facilitate expression and purification. The prolactin precursor sequence was inserted into the N terminus as a signaling peptide to anchor CB2 to the membrane and improve CB2 expression. A dominant-negative bovine Gαi1 (Gαi1_4M) construct was generated by site-directed mutagenesis to incorporate mutations S47N, G203A, E245A and A326S to decrease the affinity of nucleotide binding of Gαβγ complex (Liang et al., 2018). All three G protein complex components, Gαi1_4M, rat Gβ1 and bovine Gγ2, were cloned into pFastBac vector separately. ScFv16 coding sequence was cloned into pFastBac vector (ThermoFisher) with a GP67 signaling peptide inserted into the N terminus and a TEV cleavage site-His8 at the C terminus.

Protein complex expression, formation, and purification

Purification of scFv16 was conducted as previously described (Koehl et al., 2018) with a subtle change. Briefly, secreted scFv16 from baculovirus-infected Sf9 insect cells (Novagen) was purified using Ni-NTA and size exclusion chromatography. After balancing the pH and removing the chelating agents by Ni^{2+} and Ca^{2+}, the cell culture supernatant was loaded onto Ni-NTA. The nickel resin was first washed with 20mM HEPES pH 7.2, 100mM NaCl, 50mM imidazole for 10 column volumes and then eluted in buffer containing 250mM imidazole. The eluted sample was treated with TEV protease (homemade) followed by dialysis in 20mM HEPES pH 7.2, 100mM NaCl overnight at 4°C and then reloaded onto Ni-NTA resin to remove cleaved octa-histidine tag. The flow-through was collected and applied to a HiLoad Superdex 200, 10/60 column (GE Healthcare). The monomeric peak fractions were concentrated and fast-frozen by liquid nitrogen.

CB2, Gαi1_4M, His8-tagged Gβ1 and Gγ2 were co-expressed in Sf9 insect cells (Novagen) using the Bac-to-Bac baculovirus expression system (Invitrogen). Cell cultures were grown in ESF 921 serum-free medium (Expression Systems) at 27°C to a density of 4 × 10^6 cells $mL^{-1}$and then infected with the four types of baculoviruses expressing CB2, Gαi1_4M, His8-tagged Gβ1 and Gγ2 at the ratio of 1:1:1:1. After infection at 27°C for 48h, the cells were collected by centrifugation at 2000 rpm (ThermoFisher, H12000) for 20 min and kept frozen at −80°C for further usage.

For the purification of CB2-G_i complex, cell pellets from 1.5L culture were thawed at room temperature and suspended by French press in 20 mM HEPES pH 7.2, 50 mM NaCl, 5 mM $CaCl_2$. Complex was formed on cell membrane in the presence of 2 μM WIN 55,212-2 (Tocris) and treated with apyrase (25 mU/ml, NEB), followed by incubation for 1.5 h at room temperature. Cell membranes were collected by ultra-centrifugation at 100,000 x g for 35 min. The membranes were then re-suspended and solubilized in buffer containing 20 mM HEPES, pH 7.2, 100 mM NaCl, 5 mM $CaCl_2$, 10% Glycerol, 0.5% (w/v) dodecyl-β-D-maltoside (DDM, Anatrace), 0.15% (w/v) cholesteryl hemisuccinate TRIS salt (CHS, Anatrace), 0.5% (w/v) 3-[(3-cholamido-propyl)-dimethylammonio]-1-propanesulfonate (CHAPS, Anatrace), 0.1%(w/v) digitonin (Sigma Aldrich), 2 μM WIN 55,212-2 and 25 mU mL^{-1} apyrase for 2.5 h at 4°C. The supernatant was isolated by centrifugation at 100,000 × g for 45 min and then incubated for 3h at 4°C with pre-equilibrated 5mL FLAG resin. After batch binding, the FLAG resin with immobilized protein complex was manually loaded onto a gravity column (Bio-Rad). The resin was first washed with 10 column volumes of 20 mM HEPES, pH 7.2, 100 mM NaCl, 0.05% DDM (w/v), 0.01% CHS (w/v), 0.05% CHAPS, 0.1% digitonin(w/v), 2 μM WIN 55,212-2. Detergent was then exchanged on resin by two washing steps in 20 mM HEPES, pH 7.2, 100 mM NaCl, 2 μM WIN 55,212-2 supplemented with different detergents: first 0.02% DDM (w/v), 0.004% CHS (w/v), 0.02% CHAPS, 0.1% digitonin, then 0.1% digitonin for 10 column volumes each. Subsequently, the FLAG resin with bound material was gently resuspended in 20 mM HEPES, pH 7.2, 100 mM NaCl, 0.1% digitonin, 2 μM WIN 55,212-2, treated with TEV protease and 2.5 mg scFv16 overnight at 4°C. Released protein from FLAG beads was collected next day, concentrated and then loaded onto a Superdex 200, 10/300 GL increase column (GE Healthcare) pre-equilibrated with buffer containing 20 mM HEPES, pH 7.2, 100 mM NaCl, 0.075% digitonin, 2 μM WIN 55,212-2. The eluted fractions of monomeric complex were pooled and concentrated for cryo-EM grids preparation. The final yield of purified complex is approximately 1mg per liter of insect cell culture.

Sample preparation and EM data collection

A droplet (3.0 μl) of the purified CB2-WIN 55,212-2-G_i-scFv16 complex at a concentration of about 7.0 mg ml^{-1} was applied to a glow-discharged holey carbon grid (Quantifoil R1.2/1.3, Au 300 mesh), and subsequently vitrified using a Vitrobot Mark IV (FEI Company). Cryo-EM movie stacks were collected on a Titan Krios microscope operated at 300 kV under EFTEM mode. Nanoprobe with 0.9 μm illumination area was used. Data were recorded on a post-GIF Gatan K2 summit camera at a nominal magnification of 130,000, using super-resolution counting model at physical pixel size of 1.029 Å. BioQuantum energy filter was operated in the zero-energy-loss mode with an energy slit width of 20 eV. The total accumulative electron dose is ~83 e-/ $Å^2$ fractioned over 40 subframes with a total exposure time of 8 s. The target defocus range was set to −1.0 ~-2.5 μm. A total of 8,810 image stacks were collected with two datasets.

Image processing and 3-D reconstructions

The movie stacks were corrected for drift and beam-induced motion by MotionCor2 (Zheng et al., 2017) with 2 × binning, which generated drift-corrected summed images with and without electron-dose weighting. Each micrograph was manually inspected to remove bad pictures that were contaminated by crystalline ice or other forms of visible contamination, and CTF parameters were estimated by CTFFIND4 (Rohou and Grigorieff, 2015) using non-dose-weighted images. After sorting, micrographs with maximum estimated resolution beyond 4.0 Å were discarded, and good motion-corrected summed images with dose-weighting were used for all other image processing in RELION 3.0 (Zivanov et al., 2018) and cryoSPARC (Punjani et al., 2017). Global and local resolution estimates were calculated in RELION using the gold-standard Fourier shell correlation (FSC = 0.143) criterion (Rosenthal and Henderson, 2003). About 3.5K manually picked parties were used to generate the auto picking 2D reference. The two datasets were performed auto picking and particle extraction, separately in RELION3.0. Particles extracted from each sub-dataset were 4 times downscaled and subjected to reference-free 2D classification to remove false picks and obvious junk classes leaving behind approximately 341,033 particles from dataset1 and 627,252 particles from dataset2 (Figure S2). The selected particles were re-centered and re-extracted for further 3-D processing. The initial model was generated in cryoSPARC (Figure S2) with re-extracted particles from dataset1. The totally good 968,288 particles were 3-D classified with 8 classes in RELION3.0 with 60 Å low pass filter of the initial model. Two good classes (~812k particles) were selected for another round of 3-D classification with CB2/G_i/scFv16 mask. A final set of 772k homogeneous CB2/G_i/scFv16 complex particles was selected to perform 3-D refinements in RELION3.0. The final model was refined to an overall resolution of 3.2 Å. The map was sharpened with a B-factor of −98 $Å^2$ (Figure S3). Local resolution estimates were determined by ResMap software (Kucukelbir et al., 2014; Figure S3). The final set of homogeneous CB2/Gi/scFv16 complex particles were also subjected to AHD focused refinement to generate a better map for AHD domain (Figure S3).

Model building and refinement

The initial G_i protein and scFv16 model were adopted from the cryo-EM structure of μ-opioid receptor-G_i Protein complex (PDB: 6DDE), and initial CB2 model was generated by an online homology model building tool (Kelley et al., 2015). All models were docked into the electron microscopy density map, followed by iterative manual adjustment and rebuilding in COOT (Emsley and Cowtan, 2004), and real space refinement using Phenix programs (Adams et al., 2010). The model statistics were validated using Phenix Comprehensive validation (Adams et al., 2010). Structural figures were prepared in Chimera and PyMOL (https://pymol.org/2/). The final refinement statistics are provided in the Table S1. The extent of any model overfitting during refinement was measured by refining the final model against one of the half-maps and by comparing the resulting map versus model FSC curves with the two half-maps and the full model.

Protein thermostability assay

A fluorescence detection assay was conducted using the thiol-specific fluorochrome N-[4-(7-diethylamino-4-methyl-3-coumarinyl)-phenyl]-maleimide (CPM) to determine thermal stability of CB2-G_i-scFv16 complex. The CPM reacts with the native cysteines embedded in the protein. CPM dye (Sigma Aldrich) was dissolved at 4 mg/mL in DMSO as stock, and then diluted 1:40 with CPM dilution buffer containing 20 mM HEPES, pH 7.2, 100 mM NaCl. The protein (30–40 ng) was diluted in CPM dilution buffer supplemented with 0.1% digitonin to a final volume of 150 μL. 10 μL of the diluted dye was added and mixed together with protein sample gently. After incubation in ice for 10 min to allow fully equilibration of the reaction system, the mixture was transferred into a sub-micro quartz fluorimeter cuvette (Starna Cells, Inc.). The melting curve was recorded by heating the mixture from 20°C to 90°C with a ramp rate of 2°C/min in a Cary Eclipse Fluorescence Spectrophotometer (Agilent Technologies). The excitation wavelength was set at 387 nm and the emission wavelength was 463 nm. Data analysis was performed by Prism 7 (GraphPad), Tm were determined by fitting the curve to the Boltzmann sigmoidal equation.

Synthesis and characterization of XIE55 and XIE57

(E)-N, N-diethyl-4-(((3,4,5- trimethoxybenzyl)imino)methyl)aniline (1)

3,4,5-Trimethoxybenzylamine (1972 mg, 10 mmol) was added slowly to a solution of 4-(diethylamino) benzaldehyde (1770 mg, 10 mmol) and methanol (20 mL). The reaction mixture was stirred and refluxed for 12 hours. The reaction mixture was cooled to room temperature, and the solvent was removed by evaporation in vacuum to give the crude compound **1**, which was used in the next step without further purification.

N, N-diethyl-4-(((3,4,5-trimethoxybenzyl)amino)methyl)aniline (2)

The crude compound **1** was dissolved in methanol (20 mL), and $NaBH_4$ (570 mg, 15 mmol) was added. The mixture was stirred continuously for 12 hours at room temperature. The reaction solution was poured into water and extracted with ethyl acetate. The combined organic layers were washed with water and brine and then dried over Na_2SO_4. The residue was purified by flash chromatography (ethyl acetate/petroleum ether, 1:2) on silica gel to obtain the intermediate **2** used in the following steps.

(E)-N-(4-(diethylamino)benzyl)-2-phenyl-N-(3,4,5-trimethoxybenzyl)ethene-1-sulfonamide (XIE55)

XIE55 was prepared from the intermediate compound **2** (358 mg, 1.0 mmol) and (*E*)-2-phenylethene-1- sulfonyl chloride (202 mg, 1.0 mmol). The residue was purified by flash chromatography (ethyl acetate/petroleum ether, 1:2) on silica gel to obtain final product **XIE55**. White solid (278 mg, yield: 53%). m.p 95-97°C; ^{1}H NMR (400 MHz, DMSO-*d*6) δ7.65 (t, *J* = 2.4 Hz, 2H), 7.44–7.42 (m, 3H), 7.38 (s, 1H), 7.26 (s, 1H), 7.09 (d, *J* = 8.80 Hz, 2H), 6.59 (d, *J* = 8.40 Hz, 2H), 6.47 (s, 2H), 4.22 (s, 2H), 4.19 (s, 2H), 3.65 (s, 6H), 3.59 (s, 3H), 3.30–3.25 (m, 4H), 1.06 (t, *J* = 7.20 Hz, 6H). ^{1}H NMR (400 MHz, CDCl3) δ7.44 – 7.37 (m, 6H), 6.64 (d, *J* = 8.80 Hz, 2H), 6.56–6.502 (m, 3H), 4.28 (s, 4H), 3.85 (s, 3H), 3.82 (s, 6H), 1.18 (t, *J* = 6.80 Hz, 6H); ^{13}C NMR (600 MHz, CDCl3): δ 153.29, 147.54, 140.51, 137.37, 132.88, 131.88, 130.57, 130.47, 129.00, 128.05, 125.70, 121.63, 111.47, 105.55, 60.86, 56.10, 50.02, 49.85, 44.33, 12.54; MS (ESI): *m/z* 525.33 (M + H) $^+$.

N-(4-(diethylamino)benzyl)-N-(3,4,5-trimethoxybenzyl)thiophene-2-sulfonamide (XIE57)

XIE57 was prepared from the intermediate compound **2** (358 mg, 1.0 mmol) and thiophene-2-sulfonyl chloride (182 mg, 1.0 mmol). The residue was purified by flash chromatography (ethyl acetate/petroleum ether, 1:2) on silica gel to obtain final product **XIE57**. Yellow solid (270 mg, yield: 54%). m.p 77-80°C; ^{1}H NMR (400 MHz, DMSO-*d*6) δ 8.03–8.02 (m, 1H), 7.76–7.75 (m, 1H), 7.28–7.25 (m, 1H), 6.96 (d, *J* = 8.40 Hz, 2H), 6.55 (d, *J* = 8.80 Hz, 2H), 6.28 (s, 2H), 4.20 (s, 2H), 4.17 (s, 2H), 3.61 (s, 6H), 3.60 (s, 3H), 3.30–3.26 (m, 4H), 1.06 (t, *J* = 11.20 Hz, 6H); ^{13}C NMR (600 MHz, CDCl3): δ 153.06, 147.44, 141.71, 137.18, 131.72, 131.57, 131.33, 130.27, 127.28, 121.26, 111.36, 105.50(2C), 60.84, 56.00, 50.84, 50.73, 44.30, 12.52; MS (ESI): *m/z* 505.28 (M + H) $^+$.

CB2 radioligand competition binding assay

Nonradioactive ligands were diluted in binding buffer and supplemented with 10% dimethyl sulfoxide (DMSO) and 0.4% methylcellulose. Each assay plate well contained a total of 200 μL of reaction mixture composed of 5 μg of CB2 membrane protein, labeled [^{3}H] CP-55,940 ligand at a final concentration of 3 nM, and the unlabeled ligand at variable dilutions, as stated above. Plates were incubated at 30°C for 1 h with gentle shaking. The reaction was terminated by rapid filtration through Unifilter GF/B filter plates using a Unifilter Cell Harvester (PerkinElmer). After the plate was allowed to dry overnight, 30 μL of MicroScint-0 cocktail (PerkinElmer) was

added to each well and the radioactivity was counted using a PerkinElmer TopCounter. All assays were performed in duplicate and data points were represented as mean ± SEM. Bound radioactivity data was analyzed for Ki values using nonlinear regression analysis via GraphPad Prism 7 software.

cAMP functional assay

Cellular cAMP levels were measured according to the reported method with modifications using LANCE cAMP 384 kits (PerkinElmer) (Zhang et al., 2011; Ouyang et al., 2013). The assay is based on competition between a Europium-labeled cAMP trace complex and total cAMP for binding sites on cAMP-specific antibodies labeled with a fluorescent dye. CB_2 receptor wild-type (WT)-transfected CHO cells were seeded into a 384-well white ProxiPlates with a density of 2000 cells per well in 5 μL of RPMI-1640 medium containing 1% dialyzed FBS, 25 mM HEPES, 100 μg/mL penicillin, 100 U/ml streptomycin and 200 μg/mL of G-418. After culture overnight, 2.5 μL of cAMP antibody and RO20-1724 (final concentration, 50 μM) in stimulation buffer (DPBS 1x, containing 0.1% BSA) was added to each well, followed by addition of either 2.5 μL compound or forskolin (final 5 μM) for agonist-inhibited adenylate cyclase (AC) activity assay. After incubation at room temperature for 45 min, 10 μL of detection reagent was added into each well. The plate was then incubated for 1 h at room temperature and measured in Synergy H1 hybrid reader (BioTek) with excitation at 340 nm and emission at 665 nm. Each cAMP determination was made via at least three independent experiments, each in triplicate. EC_{50} values were determined by nonlinear regression, dose-response curves (GraphPad Prism 7).

Quantitative characterization of binding residues on CB2

Ligand binding always involves its interaction with key binding residues, the changes in the features of ligand binding site, particular rearrangements of the protein structure, etc. Thus, several key aspects of ligand binding can be explored quantitatively in a special binding region of a crystal/Cryo-EM structure, including the involved key residues, residual energy contribution, energy term, etc. Starting with the code base of the current stable version 2.2.3 of idock (Li et al., 2012; Chen et al., 2019) that adopts the exact scoring function of AutoDock Vina (Trott and Olson, 2010), we developed an even more efficient variant integrating the ability to calculate also the residual contributions of the binding energy. Our adaptation skips the CPU-intensive precalculation of free energy grid map in the case of crystal/Cryo-EM structures with a ligand bound because the need for testing a massive number of conformational candidates is no longer there. Thereafter, the program populates the precisely calculated per-atom-pair free energy for every residue and produces the results. The improvement could reduce total time consumption by 95%∼97% for most input. We will discuss this method in depth in our future publications.

Molecular docking

The docking program Surflex-Dock GeomX (SFXC) in SYBYL-X 2.0 was applied to construct receptor-ligand complexes in which the docking scores were expressed in -log10 (Kd). The main protocols or parameters of docking were addressed in our previous publications (Feng et al., 2014; Feng et al., 2015). Briefly, the docking parameters used were as follows: (a) the ''number of starting conformations per ligand'' was set to 10, and the ''number of max conformations per fragment'' was set to 20; (b) the ''maximum number of rotatable bonds per molecule'' was set to 100; (c) flags were turned on at ''pre-dock minimization,'' ''post-dock minimization,'' ''molecule fragmentation,'' and ''soft grid treatment''; (d) ''activate spin alignment method with density of search'' was set to 9.0; and (e) the ''number of spins per alignment'' was set to 12.

MD simulations

The MD simulation system consists of one copy of human CB2 transmembrane domain and the WIN 55212-2 ligand, 240 POPC (1-palmitoyl-2-oleoyl-sn-glycero-3-phosphocholine) lipids, 0.15 M NaCl, and 17082 TIP3P (Jorgensen et al., 1983) water molecules. The lipids, ions and water molecules were added using CHARMM-GUI. The detailed force field set up and MD protocol can be found elsewhere (Yin et al., 2018). In brief, protein, lipid and the ligand are described by AMBER FF14SB (Maier et al., 2015) LIPID14 (Dickson et al., 2014) and GAFF (Wang et al., 2004) force fields, respectively.

MD simulation was performed using the AMBER18 software package (Case et al., 2018). The MD system was first relaxed by a set of minimizations by removing possible steric clashes. There were three phases for the subsequent NPT (constant particle number, pressure and temperature) MD simulations: the relaxation phase (1 ns for each temperature from 50 to 250 K at a step of 50 K), the equilibrium phase (25 ns, 298 K), and the sampling phase (200 ns). 2000 snapshots were evenly selected from the sampling phase for MM-GBSA binding free energy decomposition analysis. Integration of the equations of motion was conducted at a time step of 1 fs for the relaxation phase and 2 fs for the equilibrium and sampling phases.

For each MD snapshot, the molecular mechanical (MM) energy (E_{MM}) and the MM-GB/SA solvation free energy were calculated without further minimization (Wang et al., 2006; Hou et al., 2011a, 2011b). The interaction energies between each residue and the ligand were calculated with the solvent effect being taken into account using a MM-GBSA solvation model developed previously (Hawkins et al., 1996). Key parameters controlling the MM-GBSA analyses were the following: external dielectric constant ∼80; internal dielectric constant ∼1; and the surface tension for estimating the nonpolar solvation energy ∼0.005.

Figure preparation

Structural figures were prepared in UCSF Chimera (https://www.cgl.ucsf.edu/chimera/) and PyMOL (https://pymol.org/2/).

QUANTIFICATION AND STATISTICAL ANALYSIS

All reported resolutions in cryo-EM studies are based upon the 0.143 Fourier Shell Correlation criterion. Error bars in Figure 4B represent standard error of the mean for three independent experiments.

DATA AND CODE AVAILABILITY

The accession number for the cryo-EM density map reported in this paper is Electron Microscopy Data Bank (EMDB): EMD-20470. The accession number for the CB2 model coordinates reported in this paper is Protein Data Bank (PDB): 6PT0.

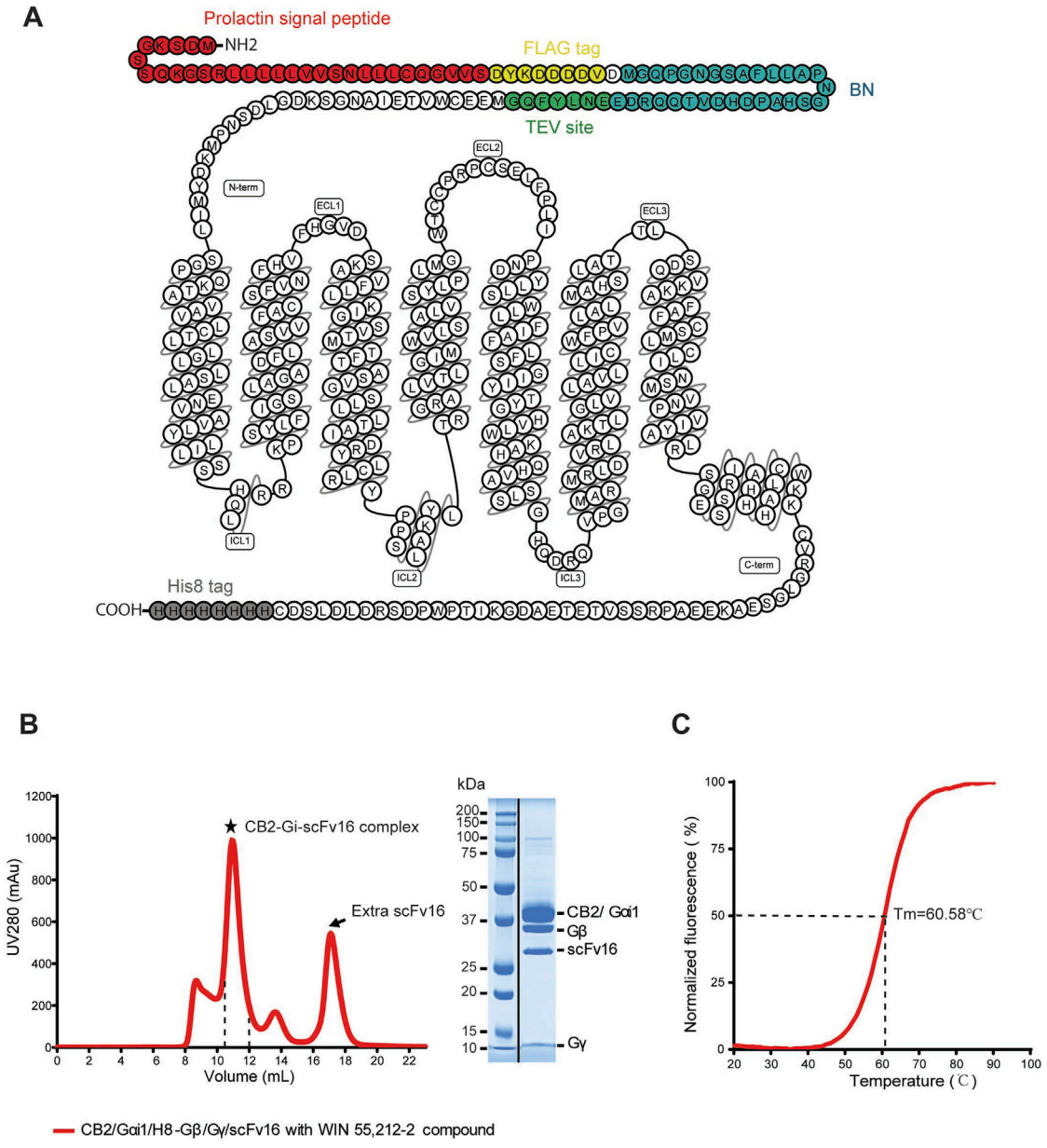

Figure S1. CB2 Construct and Complex Formation, Related to Figure 1

(A) Snake model of the CB2 construct used in this paper.

(B) Size exclusion chromatography profile and SDS-PAGE analysis of CB2-G_i-scFv16-WIN 55,212-2 complex; the peak of complex elution is marked with a star and the peak of extra scFv16 is marked with an arrow. Fractions between two dashed lines were pooled and concentrated for cryo-EM experiments. The lanes of protein marker and CB2-Gi-scFv16 complex were spliced within one gel and separated by a black vertical line.

(C) CPM assay of CB2-G_i-scFv16 activated by WIN 55,212-2 to test the half denaturing temperature, Tm value. Tm was determined by fitting the curve to Boltzmann sigmoidal equation.

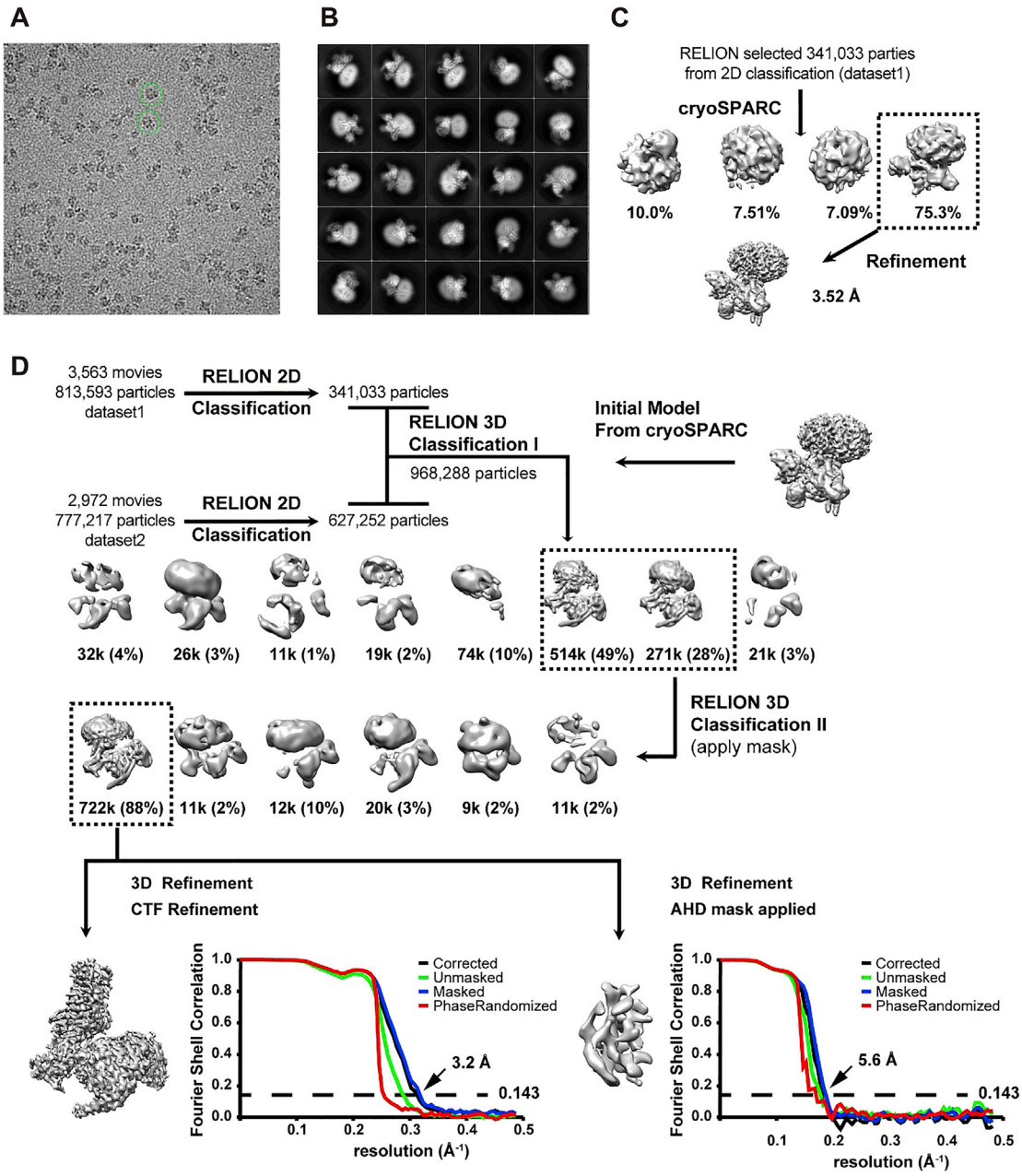

Figure S2. Cryo-EM Data Collection and Structure Determination, Related to Figure 1

(A) Representative micrographs CB2-WIN 55,212-2-G_i-scFv16 complex with particles of 190 Å diameter highlighted in a green circle.

(B) Representative images of 2D class-averages.

(C) Cryo-electron microscopy data processing workflow by cryoSPARC to generate an unbiased *Ab initio* 3D map. Boxed 3D classes were selected for further processing.

(D) Cryo-electron microscopy data processing workflow by RELION. Boxed 3D classes were selected for further processing. Half-map Fourier Shell Correlation (FSC) plots generated by RELION was shown at the down right corner. An overall resolution was set at 3.2 Å at 0.143 FSC, and the α-helical domain (AHD) focused refinement at 5.8 Å at 0.143 FSC.

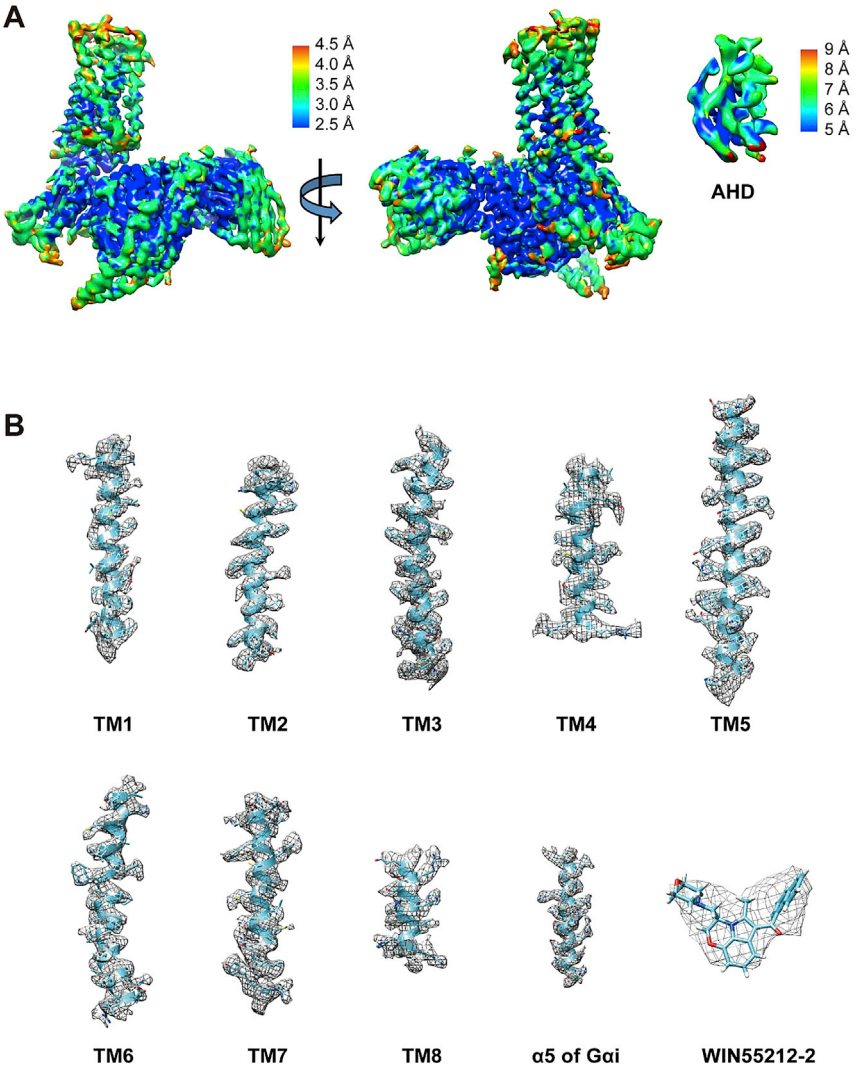

Figure S3. Cryo-EM Maps, Related to Figure 1

(A) Cryo-EM map colored according to local resolution, which was calculated from half-maps by ResMap software. The density map is shown at 0.022 contour level.

(B) Density maps of TM1-8 in CB2/WIN 55,212-2, α5 of Gαi and WIN 55,212-2 ligand, showing at 0.016 contour level.

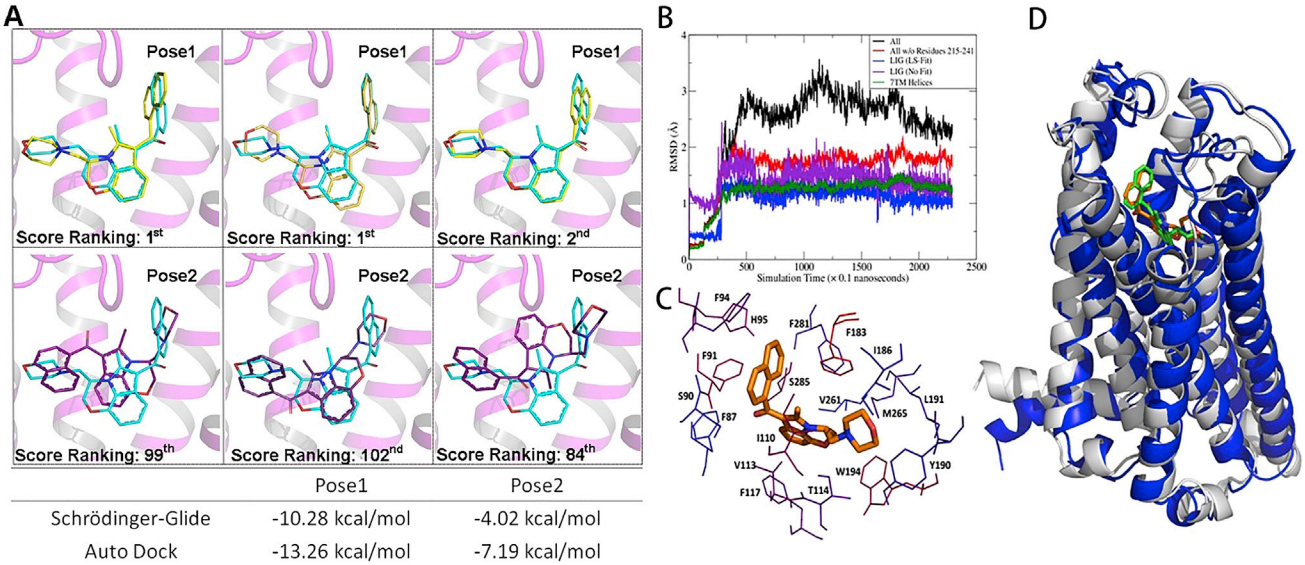

	Pose1	Pose2
Schrödinger-Glide	-10.28 kcal/mol	-4.02 kcal/mol
Auto Dock	-13.26 kcal/mol	-7.19 kcal/mol
SYBYL-Surflex Dock	-11.73 kcal/mol	-7.04 kcal/mol

Figure S4. Molecular Docking and Molecular Dynamics Simulations for the TMD (Residues 21–319), Related to Figure 2

(A) To further validate the binding pose of WIN 55,212-2, we first conducted molecular docking using three different software/algorithms, including Schrödinger-Glide (*left panels*), Auto Dock (*middle panels*), and SYBYL-Surflex Dock (*right panels*) to conduct the studies. All the docking results showed that the pose of WIN 55,212-2 presented in our manuscript (pose 1) ranked at the top one or two with lowest energy (−10.28, −13.26, and −11.73 kcal/mol, respectively) compared to the alternative pose 2 (−4.02, −7.19, and −7.04 kcal/mol, respectively).

(B) Root-mean-square deviation (RMSD) approximate time plots for all (black), all excluding the residues 215-241 loop (red), helices (green), ligand with (blue) and without (purple) least-square fitting.

(C) Hotspot residues identified by MM-GBSA decomposition. A residue is recognized as a hotspot when its interaction with the ligand is stronger than −1.0 kcal/mol. The hotspots residues according to their MM-GBSA interaction energies with the ligand are shown as brownish sticks. The stronger the interaction, the more reddish the residue is colored, while the weaker the interaction the more blueish the residue.

(D) Representative MD structure (blue cartoon and brownish sticks), having the smallest RMSD to the average structure of MD snapshots, aligned to the Cryo-EM structure (gray cartoon and greenish sticks).

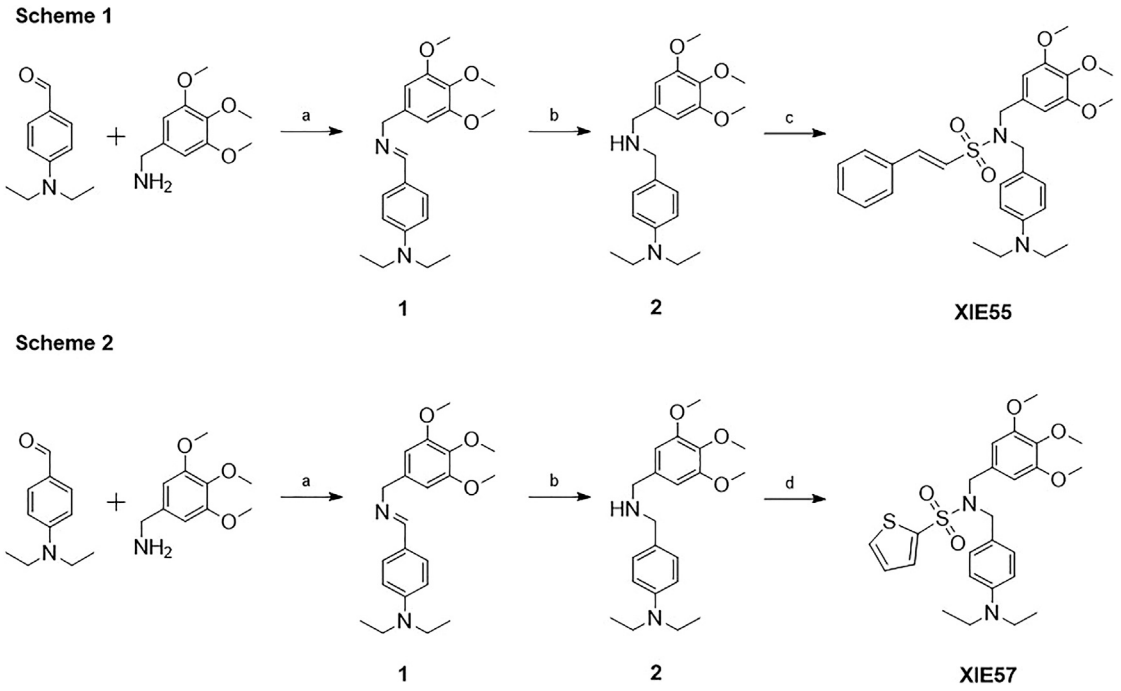

Figure S5. Synthesis of XIE55 (Scheme 1) and XIE57 (Scheme 2), Related to Figures 3C–3E, Related to Figure 4

Reagents and conditions: (a) Methanol, 70°C reflux. (b) $NaBH_4$, room temperature. (c) TEA, DCM, (E)-2-phenylethene-1- sulfonyl chloride, room temperature. (d) TEA, DCM, Thiophene-2-sulfonyl chloride, room temperature.

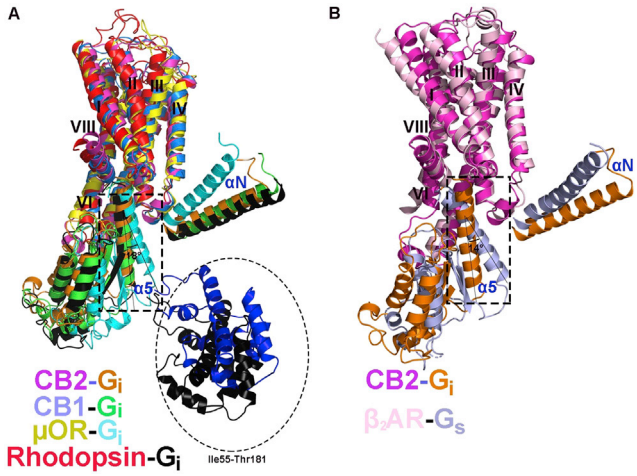

Figure S6. Relative Orientation of CB2 and G_i, Related to Figure 7

(A) Comparison of the relative orientations of G_i bound to CB2 (magenta), CB1 (PDB: 6N4B, marine), μOR (PDB: 6DDE, yellow), and Rhodopsin (PDB: 6CMO, red) when aligned on the receptor.

(B) Comparison of CB2-G_i complex with β_2AR-G_s complex (PDB:3SN6, light pink) when aligned with the receptor.

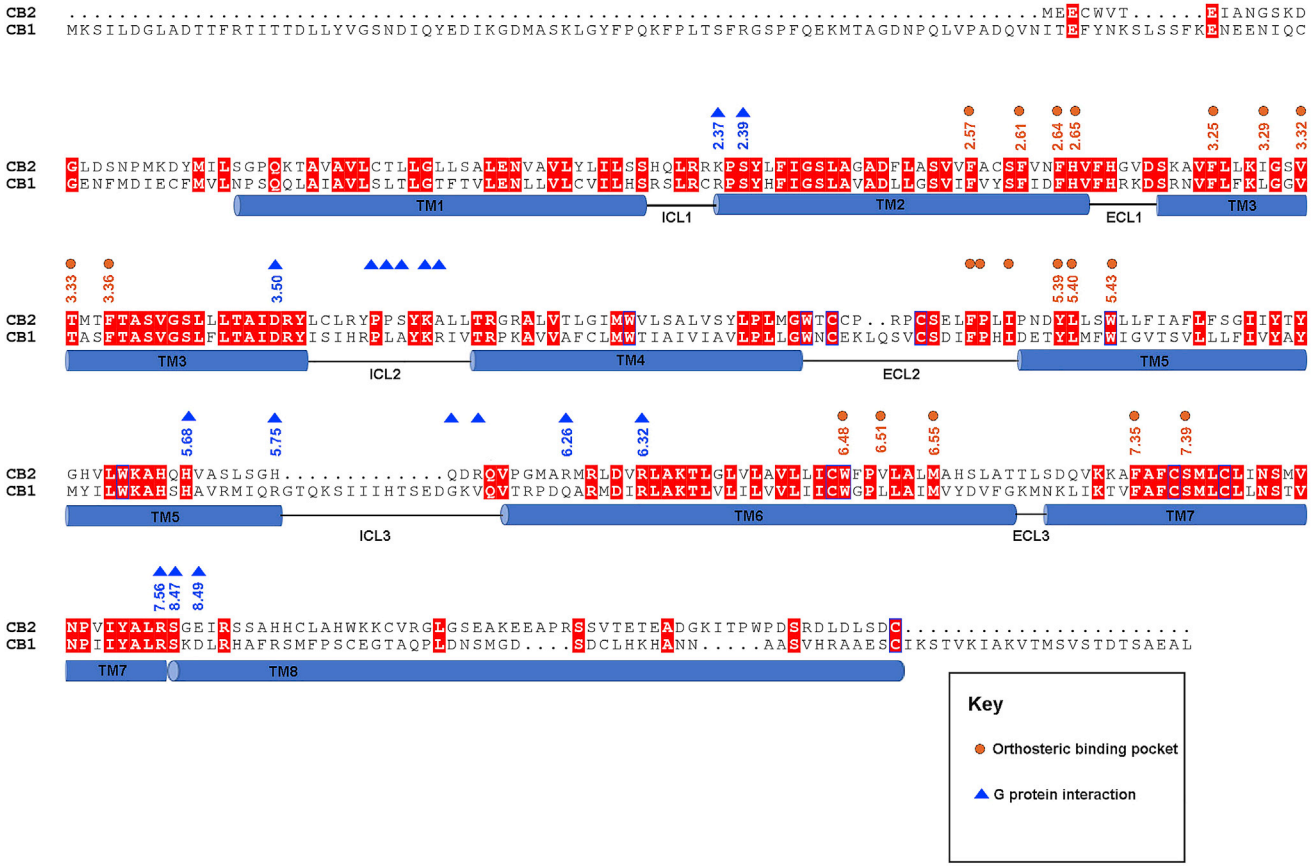

Figure S7. Common Mechanism of CB2 Activation and G Protein Coupling, Related to Figure 7

Sequence alignments between CB2 and CB1 highlight the orthosteric binding pocket residues and the TM6 kink residues for receptor activation, as well as the G_i-interface residues for G_i coupling. Secondary structure elements are annotated underneath the sequences.